DART-Lux: an unbiased and rapid Monte Carlo radiative transfer method for simulating remote sensing images

Yingjie Wang, Abdelaziz Kallel, Xuebo Yang, Omar Regaieg, Nicolas Lauret, Jordan Guilleux, Eric Chavanon, Jean-Philippe Gastellu-Etchegorry

▶ **To cite this version:**

Yingjie Wang, Abdelaziz Kallel, Xuebo Yang, Omar Regaieg, Nicolas Lauret, et al.. DART-Lux: an unbiased and rapid Monte Carlo radiative transfer method for simulating remote sensing images. Remote Sensing of Environment, 2022, 274, pp.112973. 10.1016/j.rse.2022.112973 . hal-04643523

HAL Id: hal-04643523
https://hal.science/hal-04643523

Submitted on 10 Jul 2024

HAL is a multi-disciplinary open access archive for the deposit and dissemination of scientific research documents, whether they are published or not. The documents may come from teaching and research institutions in France or abroad, or from public or private research centers.

L'archive ouverte pluridisciplinaire **HAL**, est destinée au dépôt et à la diffusion de documents scientifiques de niveau recherche, publiés ou non, émanant des établissements d'enseignement et de recherche français ou étrangers, des laboratoires publics ou privés.

DART-Lux: an unbiased and rapid Monte Carlo radiative transfer method for simulating remote sensing images

Yingjie Wang[1], Abdelaziz Kallel[3], Xuebo Yang[2], Omar Regaieg[1], Nicolas Lauret[1], Jordan Guilleux[1], Eric Chavanon[1], Jean-Philippe Gastellu-Etchegorry[1]

[1] CESBIO, CNES-CNRS-IRD-UT3, University of Toulouse, 31401 Toulouse CEDEX 09, France

[2] Aerospace Information Research Institute, Chinese Academy of Sciences, Beijing 100094, China

[3] CRNS, ATMS, Sfax, Tunisia

Correspondence to: Yingjie WANG (yingjiewang1102@gmail.com), Jean-Philippe Gastellu-Etchegorry (jean-philippe.gastellu@iut-tlse3.fr)

Abstract

Accurate and efficient simulation of remote sensing images is increasingly needed in order to better exploit remote sensing observations and to better design remote sensing missions. DART (Discrete Anisotropic Radiative Transfer), developed since 1992 based on the discrete ordinates method (*i.e.*, standard mode DART-FT), is one of the most accurate and comprehensive 3D radiative transfer models to simulate the radiative budget and remote sensing observations of urban and natural landscapes. Recently, a new method, called DART-Lux, was integrated into DART model to address the requirements of massive remote sensing data simulation for large-scale and complex landscapes. It is developed based on efficient Monte Carlo light transport

algorithms (*i.e.*, bidirectional path tracing) and on DART model framework. DART-Lux can accurately and rapidly simulate the bidirectional reflectance factor (BRF) and spectral images of arbitrary landscapes. This paper presents its theory, implementation, and evaluation. Its accuracy, efficiency and advantages are also discussed. The comparison with standard DART-FT in a variety of scenarios shows that DART-Lux is consistent with DART-FT (relative differences < 1%) with simulation time and memory reduced by a hundredfold. DART-Lux is already part of the DART version freely available for scientists (https://dart.omp.eu).

Key words

DART, Radiative transfer, Monte Carlo, Bidirectional path tracing, Remote sensing image

1 Introduction

Physically based three-dimensional (3D) models that simulate the interactions between electromagnetic radiation and the realistic terrestrial surfaces and that simulate the remotely sensed multi- and hyper-spectral images of these surfaces provide essential solutions for quantitative interpretation of remote sensing data and for the design of remote sensing missions. It explains that in the last four decades, a number of 3D radiative transfer (RT) models that can simulate the radiative and biophysical processes in 3D natural and/or urban landscape have been developed (Widlowski et al., 2015, 2013, 2007). These models can be divided into three categories according to their mathematical solution of RT equation: (i) radiosity methods, (ii) Monte Carlo methods and (iii) discrete ordinates methods.

Radiosity methods, such as DIANA (Goel et al., 1991) and RGM (Qin and Gerstl, 2000), solve the RT equation through the inversion of a square matrix that includes the geometric view factors of each surface relative to all other surfaces in the simulated scene. The advantage of

the radiosity method is that once the inverse square matrix is computed, the bidirectional reflectance factor (BRF), directional brightness temperature (DBT) and radiative budget of the scene can be easily derived. However, the major limitation is that its computation time and computer memory dramatically increase for complex scenes made of millions of facets. Also, it is less flexible to simulate other remote sensing signals such as LiDAR and polarization. Monte Carlo methods, such as FLIGHT (North, 1996), Raytran (Govaerts, 1996) and librat (Lewis, 1999), estimate the solution of RT equation by repeatedly sampling the ray paths in the scene. This stochastic process converges to the exact solution after sufficient trials and repetitions. The Monte Carlo method is usually considered as the most accurate, flexible, but also the most computer expensive solution of radiative transfer (Goel, 1988; Myneni et al., 1989). Discrete ordinates methods, such as the models of (Kimes and Kirchner, 1982; Myneni et al., 1990), DART (Gastellu-Etchegorry et al., 1996) and DIRSIG (Kraska, 1996), solve the RT equation along a finite number of discrete directions. Similar to Monte Carlo method, the discrete ordinates method is flexible to simulate the remote sensing signals and radiative budget of complex landscapes. It is known as a good compromise between accuracy and computation time.

The initial implementations of the 3D RT models in the 1980s and 1990s were usually adapted to small scale, schematic scenes, and provided limited remote sensing products (*e.g.*, BRF or image). The evolution of the remote sensing science, the ray-tracing algorithms, computer hardware and 3D representations of Earth surface elements explains the constant improvement of 3D RT models. For example, RAPID, developed on the basis of RGM, simplifies the representation of canopy by porous objects, which allows one to simulate complex vegetated scenes since only view factors between porous objects are computed and stored (Huang et al., 2013). Rayspread, a speeded up successor of Raytran, implements the variance reduction

technique called photon spreading that sends a group of virtual photons to all possible sensors after each interaction (Widlowski et al., 2006). It also provides absorption, transmission, and albedo products for studying photosynthesis and other physiological processes. The flexibility of discrete ordinates method and the increasing requirements of 3D RT modelling explain that DART and DIRSIG continuously extend their functionality for general-purpose remote sensing applications. The initial DART only simulated the BRF and images of turbid canopies in the short waves (Gastellu-Etchegorry et al., 1996). Later, it integrated a specifically designed atmospheric RT modelling module (Gascon et al., 2001) and was extended to the thermal infrared domain with the provision of 3D radiative budget of canopies (Guillevic et al., 2003). Afterwards, it integrated an additional representation of vegetation and urban elements by polygons with various surface optical properties (*e.g.*, Lambertian with specular, Hapke and RPV models) (Gastellu-Etchegorry, 2008), LiDAR and passive sensors (*e.g.*, pushbroom, airborne and in-situ camera) (Gastellu-Etchegorry et al., 2015; Yin et al., 2016), and sun induced fluorescence (SIF) (Gastellu-Etchegorry et al., 2017). Subsequently, it integrated a powerful ray-object intersection kernel Embree (Wald et al., 2014) that considerably accelerated it up to factors of ~300 (Qi et al., 2019b), depending on the simulated landscapes.

Despite the continuous improvements of the functionality, accuracy and efficiency of the 3D RT models, it is still challenging to simulate realistic complex canopy scenes. For example, reference models in RAMI3 (RAdiative transfer Model Intercomparison) including DART had good ~1% agreement for schematic canopies (Widlowski et al., 2007) but were less consistent for the RAMI4 realistic canopies (Widlowski et al., 2015). Indeed, simplifications of RT modelling and canopy mock-ups were likely applied by many 3D RT models to simulate the huge volumes of measurements of realistic canopies in a reasonable computer time. Taking DART as an example, the number of discrete directions was largely reduced, and the shoots of

pine trees were represented by voxels filled with turbid medium. It stresses the need to improve 3D RT models and the management of mock-ups in order to handle large-scale and complex landscapes. The advancement of physically-based Monte Carlo light transport algorithms in computer graphics aimed at rapid rendering of colour images provides solutions (Kajiya, 1986; Pharr et al., 2016; Veach, 1997). Some of them are already integrated by recent 3D RT models. For example, DIRSIG was redesigned with the path tracing approach (Goodenough and Brown, 2017; Kajiya, 1986), where a backward ray from the sensor is used to construct a stochastic path that either connects a light source or terminates on an absorbing surface. LESS uses the ray-tracer Mitsuba (Jakob, 2010; Nimier-David et al., 2019; Qi et al., 2019a), where a stochastic path is constructed either forward to simulate the BRF or backward to simulate images.

Standard DART modelling (*i.e.*, discrete ordinates method) is much less efficient than recent Monte Carlo-based models such as LESS in simulating precise images of large-scale and complex landscapes. For example, it takes more than 45 times memory and more than 20 times computation time than LESS to simulate the nadir image of the Järvselja Birch stand in RAMI4 experiment (Qi et al., 2019a). Therefore, with the goal of fast, robust and accurate RT simulations for large-scale and complex landscapes, since 2018, we have been designing a new Monte Carlo method called "DART-Lux" in DART model. It is based on the standard DART framework and the Monte Carlo algorithm (*i.e.*, bidirectional path tracing) of the open-source renderer LuxCoreRender (https://luxcorerender.org). DART-Lux efficiently combines forward and backward light transport to robustly simulate any sensor-source configuration and surface scattering function, as detailed in section 3.

Usually, light transport algorithms in computer graphics aim at producing very fast and visually pleasing colour images or videos. They work with only three bands and with low radiometric

accuracy, which is not suitable for remote sensing applications. For example, sun and atmosphere illumination in outdoor scenarios is simulated using parameterized models (Hosek and Wilkie, 2012; Preetham et al., 1999), which is very approximative compared to the atmospheric RT modelling in MODTRAN and DART (Berk et al., 1987; Grau and Gastellu-Etchegorry, 2013; Wang and Gastellu-Etchegorry, 2020). Similarly, important physical and biophysical processes, such as polarization and SIF emission, are not considered. In contrast, 3D RT models must accurately model all major radiation interactions in the atmosphere and landscapes for remote sensing applications. Therefore, three main types of development have been carried out in DART-Lux, some of them are still in progress: (1) RT modelling: SIF and thermal emission, realistic atmosphere and 3D clouds, any surface / volume scattering functions, polarization, *etc*. (2) Products: pushbroom and camera hyperspectral radiance / reflectance / brightness temperature / SIF images, 3D radiative budget, images per type of land cover (*e.g*., tree, ground), LiDAR waveform, point cloud and photon counting, polarization components, look-up-tables for inversion and sensitivity work, *etc*. (3) Computer science: accurate ray-object intersection to avoid self-intersection and watertight intersection issues (Woo et al., 1996; Woop et al., 2013)), high radiometric accuracy, GPU acceleration, distributed computing, *etc*.

This paper presents the theoretical basis, framework architecture and evaluation of DART-Lux. Section 2 summarizes the mathematical formulation of image modelling and DART framework. Section 3 details DART-Lux theoretical basis and implementation. Section 4 compares the new DART-Lux and the standard DART with schematic and realistic urban and forest landscapes. Finally, section 5 discusses results and section 6 concludes the work and highlights perspectives.

2 Background and method

2.1 Mathematical formulation of remote sensing image modelling

A major objective of 3D RT modelling is to simulate remote sensing image (Gastellu-Etchegorry et al., 1996; Kraska, 1996; Lewis, 1999; Qi et al., 2019a; Richtsmeier et al., 2001). It is a two-dimensional map of the radiation that the Earth surfaces and the atmosphere emit and scatter to remote sensing sensor. This modelling can be explicitly formulated by a Lebesgue integration (Eq. (8)) as detailed below.

2.1.1 Light transport equation

Radiation leaving a surface Σ is the sum of scattered and emitted radiation. Therefore, the exit radiance $L(r, \Omega_o)$ along direction Ω_o is the sum of emitted radiance $L_e(r, \Omega_o)$ along direction Ω_o and scattered radiance to direction Ω_o due to all incident radiance $L(r, -\Omega_i)$ from the 4π space. It leads to the light transport equation, also called rendering equation (Kajiya, 1986):

$$L(r, \Omega_o) = L_e(r, \Omega_o) + \int_{4\pi} L(r, -\Omega_i) \cdot f(r, -\Omega_i, \Omega_o) \cdot \cos\theta_i \, d\Omega_i \quad (1)$$

with θ_i the incident angle (Figure 1.a) and $f(r, -\Omega_i, \Omega_o)$ the bidirectional scattering distribution function (BSDF) of surface Σ that is the bidirectional reflectance distribution function (BRDF) $\frac{\rho(r, -\Omega_i, \Omega_o)}{\pi}$ or the bidirectional transmittance distribution function (BTDF) $\frac{\tau(r, -\Omega_i, \Omega_o)}{\pi}$, depending on the relative configuration of the incident and exit directions (Eq. (2)).

$$f(r, -\Omega_i, \Omega_o) = \begin{cases} \dfrac{\rho(r, -\Omega_i, \Omega_o)}{\pi}, & \text{if } \langle \boldsymbol{n} \cdot \Omega_o \rangle \cdot \langle \boldsymbol{n} \cdot \Omega_i \rangle \geq 0 \\ \dfrac{\tau(r, -\Omega_i, \Omega_o)}{\pi}, & \text{otherwise} \end{cases} \quad (2)$$

Because solid angles depend on surface area, Eq. (1) is expressed in an area form (Eq. (3)) where an integral over all scene surfaces A replaces the integral over angular space (Figure 1.b)

$$L(r' \to r) = L_e(r' \to r) + \int_A L(r'' \to r') \cdot f(r'' \to r' \to r) \cdot G(r' \leftrightarrow r'') dA(r'') \qquad (3)$$

with $r \in A(r) \subseteq A$ a point on a surface whose BSDF is $f(r'' \to r' \to r)$. $G(r' \leftrightarrow r'') = V(r' \leftrightarrow r'') \cdot \frac{\cos\theta_i^{r'} \cdot \cos\theta_o^{r''}}{\|r'' - r'\|^2}$ is a geometric term, with $V(r' \leftrightarrow r'')$ the visibility function between r' and r'', $\theta_i^{r'}$ is the incident angle at r' and $\theta_o^{r''}$ is the exit angle at r''. $V(r' \leftrightarrow r'') = 1$ if there is nothing between r' and r'', and 0 otherwise.

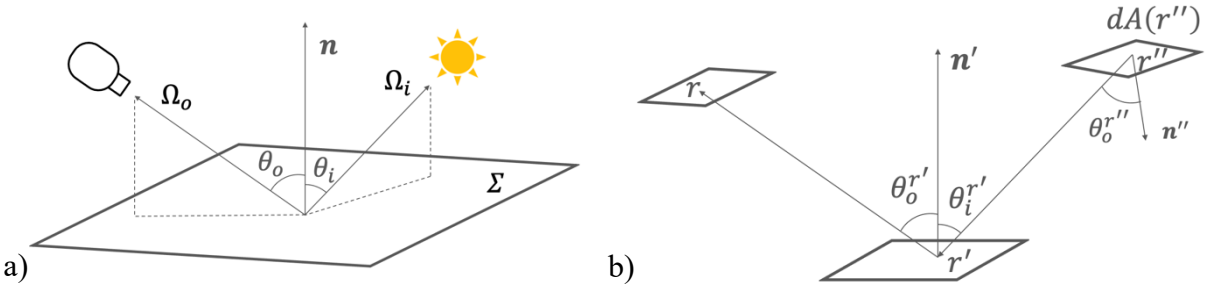

Figure 1. a) BSDF $f(r, -\Omega_i, \Omega_o)$ of a surface Σ of normal $\boldsymbol{n}$: exit radiance along direction Ω_o due to the scattering of incident irradiance along direction $-\Omega_i$. Incident angle θ_i is the angle between Ω_i and $\boldsymbol{n}$, exit angle θ_o is the angle between Ω_o and $\boldsymbol{n}$. (b) Three-point method: a ray starts from r'' on $dA(r'')$ is intercepted at r', then is scattered to r.

2.1.2 Path integral of light transport equation

In a scene with no media between surfaces, the incident radiance on a surface is the exit radiance from previous surface. Therefore, Eq. (3) can be incrementally expanded to an infinite sum of multiple-dimensional integration (Eq. (4)) with r_0 a vertex on the sensor lens, r_1 a previous vertex, and so on. Each term is the result of emitted radiance $L_e(r_n \to r_{n-1})$ after (n - 1) scattering events:

$$
\begin{aligned}
L(r_1 \to r_0) = L_e(r_1 \to r_0) &+ \int_A L_e(r_2 \to r_1) \cdot f(r_2 \to r_1 \to r_0) \cdot G(r_1 \leftrightarrow r_2) dA(r_2) \\
&+ \int_A \int_A L_e(r_3 \to r_2) \cdot f(r_3 \to r_2 \to r_1) \cdot G(r_2 \leftrightarrow r_3) \cdot f(r_2 \to r_1 \to r_0) \\
&\cdot G(r_1 \leftrightarrow r_2) dA(r_3) dA(r_2) \\
&+ \int_A \int_A \int_A L_e(r_4 \to r_3) \cdot f(r_4 \to r_3 \to r_2) \cdot G(r_3 \leftrightarrow r_4) \\
&\cdot f(r_3 \to r_2 \to r_1) \cdot G(r_2 \leftrightarrow r_3) \cdot f(r_2 \to r_1 \to r_0) \\
&\cdot G(r_1 \leftrightarrow r_2) dA(r_4) dA(r_3) dA(r_2) + \cdots
\end{aligned} \tag{4}
$$

183 Eq. (4) can be rewritten as:

$$
L(r_1 \to r_0) = \sum_{n=1}^{\infty} L(\bar{r}_n) \tag{5}
$$

184 with $L(\bar{r}_n)$ the radiance from r_1 to r_0 integrated over all paths of length *n*, *i.e.*, path with *n* edges
185 and *n* + 1 vertices, vertex r_n on the light source and vertex r_0 on the sensor lens. $\bar{r}_n = r_0 r_1 \dots r_n$
186 with $r_{k=0,1,\dots,n} \in A$, and $\bar{r}_n \in$ path space $\mathcal{D}_n$ ($n \in \mathbb{N}^*$) with $\mathcal{D}_n$ the set of paths of length *n*.
187 Figure 2 shows a path of length 4. If *n* = 1, we have $L(\bar{r}_1) = L_e(r_1 \to r_0)$. If *n* > 1, we have

$$
\begin{aligned}
L(\bar{r}_n) = \int_A f(r_2 \to r_1 \to r_0) \cdot G(r_1 \leftrightarrow r_2) \int_A \cdots \int_A f(r_{n-1} \to r_{n-2} \to r_{n-3}) \\
\cdot G(r_{n-2} \leftrightarrow r_{n-1}) \cdot \int_A L_e(r_n \to r_{n-1}) \cdot f(r_n \to r_{n-1} \to r_{n-2}) \\
\cdot G(r_{n-1} \leftrightarrow r_n) dA(r_n) dA(r_{n-1}) \cdots dA(r_2)
\end{aligned} \tag{6}
$$

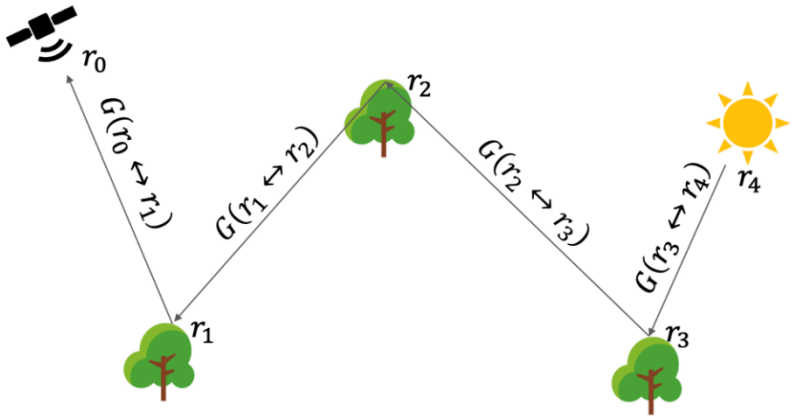

Figure 2. Path of length 4. It starts from light source at r_4, is successively scattered at r_3, r_2, r_1, and finally reaches the sensor at r_0.

2.1.3 Instrumental characteristics

Figure 3 illustrates an example of pinhole camera. Radiation incident on pixel j is transferred to radiance measurement $L^{(j)}$ (Eq. (7)) using an importance function $W_e(r_0, \Omega_0)$ (Nicodemus, 1978) whose expression depends on the instrumental characteristics (*cf.* appendix A).

$$L^{(j)} = \int_{A_0} \int_{\Delta\Omega_0} {W_e}^{(j)}(r_0, \omega_0) \cdot L(r_1 \rightarrow r_0) \cdot \cos\theta_i^{r_0} \, d\Omega_0 dA(r_0) \qquad (7)$$

with ${W_e}^{(j)}(r_0, \Omega_0) = 0$ if the incident ray is outside pixel j. $\theta_i^{r_0}$ is the angle between the incident direction and the principal optical axis. $\Delta\Omega_0$ is the solid angle that encloses all directions of the measured incident rays. $A_0 \equiv A(r_0)$ is the lens area.

In Eq. (7) expanded with the expression of $L(r_1 \rightarrow r_0)$ in Eq. (4), W_e and L_e are interchangeable which means that W_e can be treated as an exit term in the same way as L_e (Christensen et al., 1993). It gives the theoretical basis to backward light transport that is symmetric to the forward light transport. Appendix B gives a mathematical formulation of backward light transport.

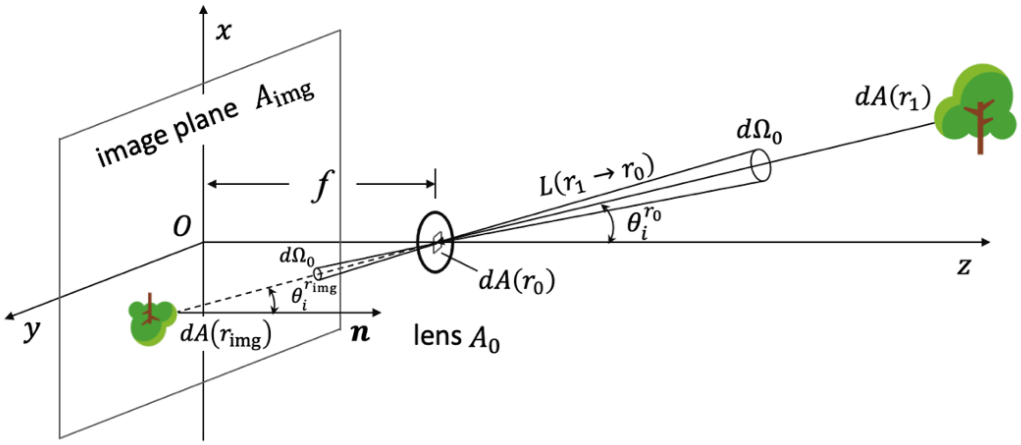

Figure 3. Pinhole camera. The lens with area A_0 is at a distance f in front of the image plane of normal $\boldsymbol{n}$. Radiation from a differential surface $dA(r_1)$ in the scene along direction $r_1 \to r_0$ is focused by the lens onto the differential surface $dA(r_{\text{img}})$ in the image plane.

2.1.4 Mathematical formulation of radiance measurement

The expanded form of Eq. (7) can be expressed in the more compact form:

$$L^{(j)} = \int_{\mathcal{D}} f^{(j)}(\bar{r})\, d\mu(\bar{r}) \tag{8}$$

with $f^{(j)}(\bar{r})$ the measurement contribution at pixel j and μ the area-product measure, $\mu(\mathcal{D}_n) = \int_{\mathcal{D}_n} d\mu(\bar{r}_n) = \int_{\mathcal{D}_n} dA(r_n) \cdot dA(r_{n-1}) \ldots dA(r_0)$. $\bar{r}$ is a path linking light source and sensor, $\bar{r} \in \mathcal{D}$ path space and $\mathcal{D} = \bigcup_{n=1}^{\infty} \mathcal{D}_n$. For path $\bar{r}_n$, $f^{(j)}(\bar{r}_n)$ is defined as:

$$\begin{aligned} f^{(j)}(\bar{r}_n) = {} & L_e(r_n \to r_{n-1}) \cdot G(r_0 \leftrightarrow r_1) \cdot W_e{}^{(j)}(r_0 \to r_1) \\ & \cdot \prod_{k=2}^{n} f(r_k \leftrightarrow r_{k-1} \leftrightarrow r_{k-2}) \cdot G(r_{k-1} \leftrightarrow r_k) \end{aligned} \tag{9}$$

The notation $f(r_k \leftrightarrow r_{k-1} \leftrightarrow r_{k-2})$ underlines the reciprocity of BSDF.

The contribution $\int_{\mathcal{D}_n} f^{(j)}(\bar{r}_n) d\mu(\bar{r}_n)$ due to the $(n-1)$th scattering order is denoted as $C_{\mathcal{D}_n}$. Then, $C_{\mathcal{D}_1}$ represents the contribution of direct illumination, $C_{\mathcal{D}_2}$ represents the contribution of first order scattering, and so on. The radiance measurement is simply the sum of $C_{\mathcal{D}_n}$ terms:

$$L^{(j)} = \int_{\mathcal{D}} f^{(j)}(\bar{r})\, d\mu(\bar{r}) = \sum_{n=1}^{\infty} C_{\mathcal{D}_n} \tag{10}$$

2.2 DART model and its framework

DART (https://dart.omp.eu) is one of the most accurate and comprehensive 3D RT models in the remote sensing community (Gastellu-Etchegorry et al., 2015, 1996). It simulates the radiative budget, BRF, radiometric (*i.e.*, radiance, reflectance, brightness temperature) images (Eq. (8)) of 3D natural and urban scenes from visible to thermal infrared domain. Its standard iterative discrete ordinates method, called DART-FT, tracks radiation along N discrete directions $\{\Omega_n\}_{n=1,2,\ldots,N}$. Radiation intercepted in iteration k is scattered to N discrete directions in iteration $k+1$. All radiation scattered in iteration k to a sensor contributes to $C_{\mathcal{D}_{k+1}}$ (Eq. (10)) (Gastellu-Etchegorry et al., 1996). DART-FT had good agreement compared to the other five benchmark models (*i.e.*, drat, FLIGHT, Rayspread, Raytran, SPRINT) in RAMI3 experiment with 1% difference on average (Widlowski et al., 2007). It was also successfully evaluated with the satellite, airborne and ground-based measurements which indicated a RMSE about 0.02 on reflectance (Janoutová et al., 2019) and less than 2 K on brightness temperature (Guillevic et al., 2003; Sobrino et al., 2011). DART also has a complete framework for 3D RT modelling and for remote sensing and radiative budget applications (Gastellu-Etchegorry et al., 2015), with specific input data, processing modules and output data (Figure 4).

Input data. Input data set up all the parameters to run a DART simulation. A graphical user interface (GUI) allows one to import / manage 3D objects and digital elevation models (DEM), define and assign optical and temperature properties, configure the atmosphere (geometry, vertical profile and optical properties of gas, aerosol and/or cloud), select the RT modelling method (*e.g.*, discrete ordinates, Monte Carlo) and the products. All input parameters are encoded in extensible markup language (XML) to ease data access.

Processing modules. Four major modules process input data to simulate products. (1) Direction: it subdivides the 4π space into *N* user-defined discrete directions for ray tracking. (2) Phase: it computes band optical properties, temperature properties, and scattering phase functions of turbid and fluid (gas, aerosol, cloud, soots, *etc*.) volumes. (3) Mock-up: it creates the 3D mock-up of the landscape and atmosphere, assigns temperature and optical properties per scene element, and computes atmosphere vertical profiles (pressure, temperature, density). (4) Dart: it simulates the RT in the landscape and in the atmosphere with a selected modelling method and generates the requested products.

Output data. Two types of products are simulated. (1) Remote sensing signal: satellite/airborne/in-situ radiometric images, BRF/DBT, LiDAR signal, SIF, *etc*. (2) Radiative budget: 1D/2D/3D distribution of intercepted, absorbed, scattered and emitted (*i.e*., thermal emission, SIF) radiation. All products can be stored per type of scene element (*e.g*., leaf, trunk) and in a look-up-table. In addition, DART also generates geometric products such as digital surface model, area per type of scene element, leaf area index, *etc*.

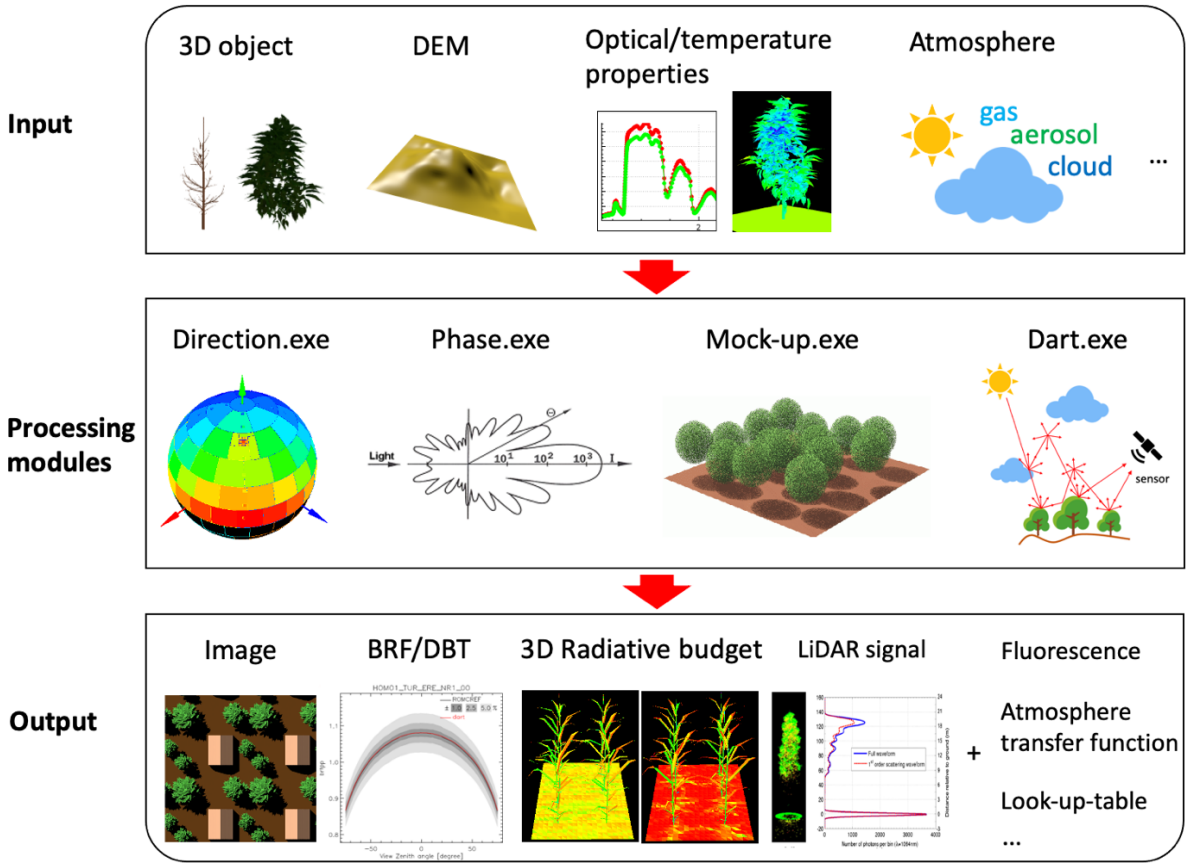

Figure 4. DART framework. Its four modules (Direction, Phase, Mock-up, Dart) simulate remote sensing and radiative budget products for any instrumental / experimental configurations.

3 A new Monte Carlo method DART-Lux

3.1 Presentation

Monte Carlo methods (Weinzierl, 2000) can assess the high-dimensional integral form of $L^{(j)}$ in Eq. (8). For example, a random path $\bar{R} \in \mathcal{D}$ sampled according to a choosing probability density function (PDF) $p(\bar{r})$, can give an unbiased estimate of $L^{(j)}$:

$$F^{(j)} = \frac{f^{(j)}(\bar{R})}{p(\bar{R})} \tag{11}$$

with expected value $\mathbb{E}\left(F^{(j)}\right) = \int_{\mathcal{D}} \frac{f^{(j)}(\vec{r})}{p(\vec{r})} p(\vec{r})\, d\mu(\vec{r}) = \int_{\mathcal{D}} f^{(j)}(\vec{r})\, d\mu(\vec{r}) = L^{(j)}$.

The remote sensing images can be accurately and efficiently simulated under two conditions: (1) path samples are generated quickly, and (2) an optimised estimator speeds up the convergence. To meet these conditions, the new Monte Carlo method, called DART-Lux (Figure 5) is designed based on the bidirectional path tracing (BDPT) algorithm (Lafortune and Willems, 1993; Veach and Guibas, 1995a, 1995b). It estimates the radiance measurement $L^{(j)}$ by sampling a set of paths and summing up their weighed contributions (Figure 5). This section details its theoretical basis: path creation method, evaluation of radiance measurement, and its light and sensor models.

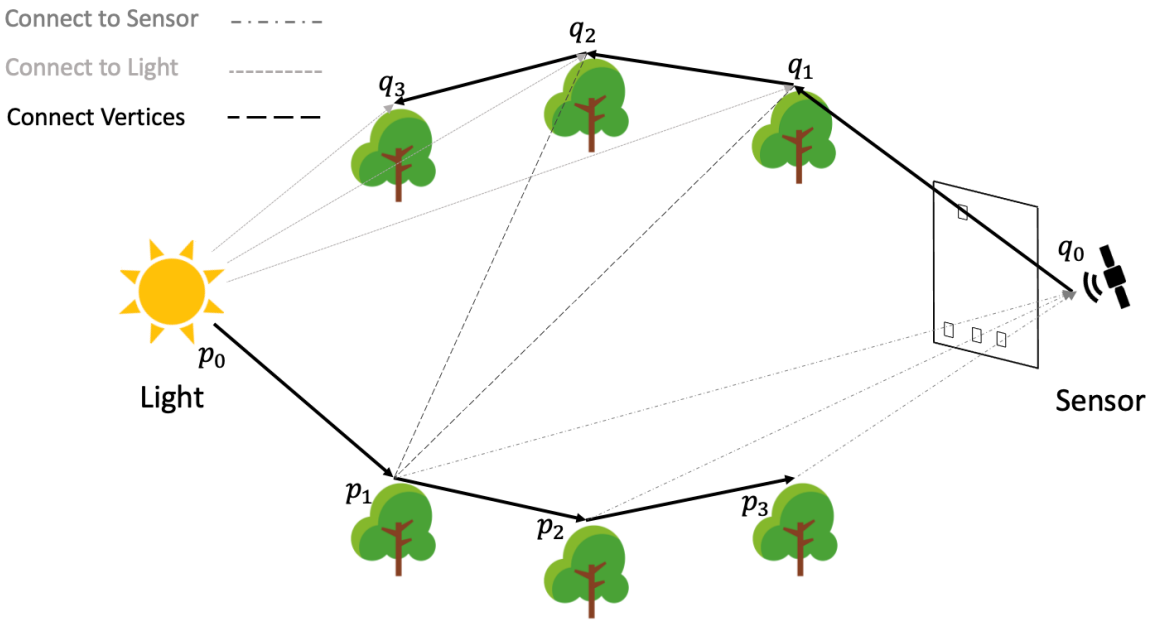

Figure 5. DART-Lux bidirectional path tracing with $N_v = 4$ vertices (maximal scattering order 3). Random walks start from the light source and sensor. $\bar{p}_4 = p_0, p_1, p_2, p_3$ is a light sub-path (random walk from light source). $\bar{q}_4 = q_0, q_1, q_2, q_3$ is a sensor sub-path (random walk from sensor). A set of paths is generated by connecting a vertex of light sub-path and a vertex of sensor sub-path. An intersection test is done at each connection. Three methods can connect vertices. 1) Connect to light: a sensor sub-path vertex is connected to a newly sampled vertex on the light source. 2) Connect to sensor: a light sub-path vertex is connected to a newly sampled vertex on the sensor lens and mapped to the image plane. 3) Connect vertices: a light

sub-path vertex in the scene is connected to a sensor sub-path vertex in the scene. Note that a light sub-path can randomly hit the sensor lens, and a sensor sub-path can randomly hit the light source.

3.2 Efficient path sampling

3.2.1 Direction and vertex sampling

At each scattering event, a random scattered direction is sampled according to the distribution of scattering power due to unit incident power. Eq. (12) defines the PDF of an exit direction Ω_o knowing the incident direction $-\Omega_i$, using the importance sampling method (Kahn and Marshall, 1953). The probability of reflection P^* is 1 for opaque surfaces (transmittance $\tau = 0$), 0 for non-reflective surfaces (reflectance $\rho = 0$), and 0.5 otherwise ($\rho, \tau > 0$) which makes the sampling less dependent on spectral properties. The PDF $p(\Omega_i | -\Omega_o)$ for sensor sub-path sampling can be derived similarly.

$$p(\Omega_o|-\Omega_i) = \begin{cases} \mathrm{P}^* \cdot \dfrac{\dfrac{\rho(r,-\Omega_i,\Omega_o)}{\pi} \cdot \cos\theta_o}{\int_{2\pi} \dfrac{\rho(r,-\Omega_i,\Omega_o')}{\pi} \cdot \cos\theta_o' \, d\Omega_o'}, & \text{if } (\boldsymbol{n}\cdot\Omega_o)\cdot(\boldsymbol{n}\cdot\Omega_i) \geq 0 \\ (1-\mathrm{P}^*) \cdot \dfrac{\dfrac{\tau(r,-\Omega_i,\Omega_o)}{\pi} \cdot \cos\theta_o}{\int_{2\pi} \dfrac{\tau(r,-\Omega_i,\Omega_o')}{\pi} \cdot \cos\theta_o' \, d\Omega_o'}, & \text{otherwise} \end{cases} \tag{12}$$

For a Lambertian surface (*i.e.*, $\rho(r,-\Omega_i,\Omega_o) = \rho$, $\tau(r,-\Omega_i,\Omega_o) = \tau$), we have:

$$p(\Omega_o|-\Omega_i) = \begin{cases} \mathrm{P}^* \cdot \dfrac{\cos\theta_o}{\pi}, & \text{if } (\boldsymbol{n}\cdot\Omega_o)\cdot(\boldsymbol{n}\cdot\Omega_i) \geq 0 \\ (1-\mathrm{P}^*) \cdot \dfrac{\cos\theta_o}{\pi}, & \text{otherwise} \end{cases} \tag{13}$$

Once a scattering direction is sampled, an intersection test along the sampled direction determines the next path vertex. Sections 3.4 details the vertex and direction samplings on the light source and sensor.

3.2.2 Bidirectional random walk

By repeatedly sampling vertices in the scene, the BDPT method (Figure 5) creates two random walks with N_v vertices each. A random walk starts from the light source and gives a light sub-path $\bar{p}_{N_v} = p_0, p_1, \ldots, p_{N_v-1}$ with vertex p_0 on the light source. A second one starts from the sensor and gives a sensor sub-path $\bar{q}_{N_v} = q_0, q_1, \ldots, q_{N_v-1}$ with vertex q_0 on the sensor lens.

3.2.3 Path generating ways

An end-to-end path $\bar{r}_{s,t}$ is generated by connecting a light sub-path $\bar{p}_s = p_0, p_1, \ldots, p_{s-1}$ and a sensor sub-path $\bar{q}_t = q_0, q_1, \ldots, q_{t-1}$ with $s, t \in [0, N_v]$.

$$\bar{r}_{s,t} = \bar{p}_s, \bar{q}_t = p_0, p_1, \ldots, p_{s-1}, q_{t-1}, q_{t-2}, \ldots, q_0 \quad (14)$$

Vertex q_{t-1} is on the light source if $s = 0$. Vertex $p_{s-1}$is on the sensor lens if $t = 0$. Any path of length n (*i.e.*, s + t = n + 1 vertices) can be created in $n + 2$ ways. For example, Figure 6 shows the five ways to create a path of length 3.

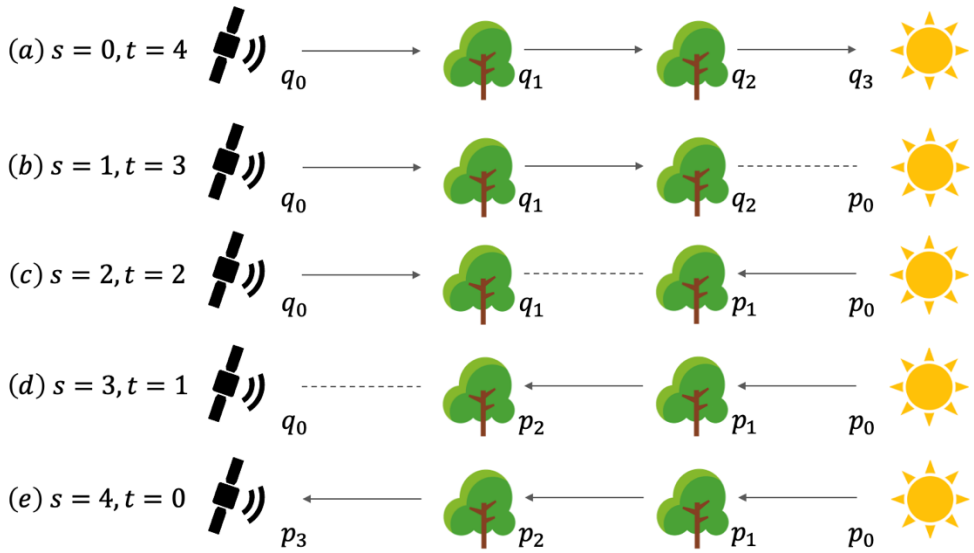

Figure 6. Five ways to generate a path of length 3. (a) Hit light: a ray starts from a sensor, is scattered twice in the scene, then hits a light source. (b) Connect to light: a ray starts from a sensor, is scattered once in the scene, then intersects a scene element from which a path is created by an explicit intersection test between the intersect vertex and a light source. (c) Connect vertices: 2

rays start from a sensor and light source, are intercepted by the scene, and a path is created by an intersection test between the two intersect vertices. (d) Connect to sensor: a ray starts from a light source, is scattered once in the scene, and intersects a scene element from which a path is created by an explicit intersection test between the intersect vertex and a sensor. (e) Hit sensor: a ray starts from a light source, is scattered twice in the scene and hits a sensor.

3.3 Measurement evaluation

3.3.1 MIS estimator of radiance measurement

The contribution $C_{\mathcal{D}_{n-1}}$ of a path of length n can be estimated with Eq. (11) using one of $n + 2$ ways (*cf.* section 3.2.3). For example, the backward light transport applies the "connect to light" way (Figure 6.(b)), and the forward light transport applies the "connect to sensor" way (Figure 6.(d)). However, the performance of path generation depends on the light source and sensor configurations, surface scattering properties, as well as the 3D structure of the landscape. For example, the "hit light" way is not efficient for sunlight because the probability to hit the sun is very small, while it is efficient for diffuse light from the sky. The "connect to light" way is efficient for Lambertian surfaces and not efficient for glossy surfaces. Hence, to robustly handle a variety of scenarios, contributions of the $n + 2$ ways are weighted and summed. For example, in the "hit light" case, we can assign a small weight if the light source is sunlight and assign a larger weight if the light source is the sky. This combined weighting method, called the multiple importance sampling (MIS) (Veach and Guibas, 1995b), uses a MIS weight $w_{s,t}$ per path $\bar{r}_{s,t}$:

$$F_{\mathrm{MIS}}^{(j)} = \sum_{s\geq 0}\sum_{t\geq 0} w_{s,t}\left(\bar{r}_{s,t}\right)\cdot\frac{f^{(j)}\left(\bar{r}_{s,t}\right)}{p\left(\bar{r}_{s,t}\right)} \tag{15}$$

Two conditions must be met to get an unbiased estimate for path of length n: $\sum_{s=0,t=n-s+1}^{n+1} w_{s,t}\left(\bar{r}_{s,t}\right) = 1$ if $f^{(j)}\left(\bar{r}_{s,t}\right) \neq 0$, and $w_{s,t}\left(\bar{r}_{s,t}\right) = 0$ if $p\left(\bar{r}_{s,t}\right) = 0$.

Eq. (15) gives the radiance measurement of infinite scattering order although infinite scattering order cannot be simulated explicitly. Usually, the contribution $C_{\mathcal{D}_n}$ in Eq. (10) decreases exponentially with scattering order (Kallel, 2018). If after scattering order M (M depends on spectral band, landscape complexity and scene optical properties), the contribution of higher scattering order is negligible, *i.e.*, $\varepsilon_M = \sum_{n=M+2}^{\infty} C_{\mathcal{D}_n} \ll L^{(j)}$, and we use the approximation:

$$L^{(j)} = C_{\mathcal{D}_1} + C_{\mathcal{D}_2} + \cdots + C_{\mathcal{D}_{M+1}} \tag{16}$$

The maximal scattering order M is a DART parameter: paths of length larger than $M+1$ are ignored, which is consistent with scattering order M. The MIS estimator of $L^{(j)}$ in Eq. (16) is:

$$F_{\text{MIS}}^{(j)} = \sum_{n=1}^{M+1} \sum_{s=0}^{n+1} w_{s,t}(\bar{r}_{s,t}) \cdot \frac{f^{(j)}(\bar{r}_{s,t})}{p(\bar{r}_{s,t})} \tag{17}$$

with

$$w_{s,t}(\bar{r}_{s,t}) = \frac{\left(p(\bar{r}_{s,t})\right)^2}{\sum_{s'=0,t'=n-s'+1}^{n+1} \left(p(\bar{r}_{s',t'})\right)^2} \tag{18}$$

Here $s + t = s' + t' = n + 1$ is always ensured. Appendix C details the incremental computation of Eq. (18) along the random walk.

3.3.2 Computation of unweighted contribution $\frac{f^{(j)}(\bar{r}_{s,t})}{p(\bar{r}_{s,t})}$

The so-called "unweighted contribution" is the estimate of corresponding path generating way (*cf.* section 3.2.3) using Eq. (11), *i.e.*, $\frac{\text{measurement contribution function } f^{(j)}(\bar{r}_{s,t})}{\text{path PDF } p(\bar{r}_{s,t})}$.

Measurement contribution function $f^{(j)}(\bar{r}_{s,t})$. It is the integrand in Eq. (8).

$$\begin{aligned} f^{(j)}(\bar{r}_{s,t}) = L_e(p_0 \to p_1) \cdot T(\bar{p}_s) \cdot f(p_{s-2} \leftrightarrow p_{s-1} \leftrightarrow q_{t-1}) \cdot G(p_{s-1} \leftrightarrow q_{t-1}) \\ \cdot f(p_{s-1} \leftrightarrow q_{t-1} \leftrightarrow q_{t-2}) \cdot T(\bar{q}_t) \cdot {W_e}^{(j)}(q_0 \to q_1) \end{aligned} \tag{19}$$

with throughputs $T(\bar{p}_s)$ and $T(\bar{q}_t)$ computed incrementally along the random walks:

$$T(\bar{p}_s) = \prod_{k=1}^{s-1} f(p_{k-2} \leftrightarrow p_{k-1} \leftrightarrow p_k) \cdot G(p_{k-1} \leftrightarrow p_k)$$
$$T(\bar{q}_t) = \prod_{k=1}^{t-1} f(q_k \leftrightarrow q_{k-1} \leftrightarrow q_{k-2}) \cdot G(q_{k-1} \leftrightarrow q_k) \quad (20)$$

The virtual BSDFs $f(p_{-1} \leftrightarrow p_0 \leftrightarrow p_1)$ and $f(q_1 \leftrightarrow q_0 \leftrightarrow q_{-1})$ are introduced to simplify the mathematical formulation. They are set to 1. $f(\bar{r}_{0,t}) = L_e(q_{t-1} \to q_{t-2}) \cdot T(\bar{p}_t) \cdot W_e^{(j)}(q_0 \to q_1)$ if $s = 0$ and $f(\bar{r}_{s,0}) = L_e(p_0 \to p_1) \cdot T(\bar{p}_s) \cdot W_e^{(j)}(p_{s-1} \to p_{s-2})$ if $t = 0$.

Path probability density $p(\bar{r}_{s,t})$. In the random walk (*i.e.*, Monte Carlo Markov chain), a stochastic exit direction depends only on the local incident direction. As a result, the PDF $p(p_k|p_{k-1}, p_{k-2})$ of vertex p_k depends only on the two previous vertices p_{k-1} and p_{k-2} and the PDF of a path is the product of the PDF of all its vertices (Eq. (21)).

$$p(\bar{r}_{s,t}) = p(\bar{p}_s) \cdot p(\bar{p}_t) = \prod_{k=0}^{s-1} p(p_k|p_{k-1}, p_{k-2}) \cdot \prod_{k=0}^{t-1} p(q_k|q_{k-1}, q_{k-2}) \quad (21)$$

3.4 Light and sensor models

3.4.1 light sources

DART-Lux is flexible to integrate a variety of light sources (*e.g.*, sun, sky, moon, LiDAR). Here, the modelling of sunlight and light from the sky is presented. The light from the sky is the light scattered downwards by the atmosphere. If more than one light source is simulated, the light sources are sampled according to their power. The sunlight can be parallel or within a cone and the sky light can be isotropic or anisotropic. In both cases, light is uniformly emitted from a virtual disk A_{disk} that is the projection of the scene sphere along the illumination

direction, *i.e.*, PDF of the first vertex on the light source is $p(p_0) = \frac{1}{A_{\text{disk}}}$. The so-called scene sphere is the sphere with minimum radius R that encloses all the scene (Figure 7). The light direction is sampled according to the energy angular distribution. The emitted radiance $L_e(p_0, \Omega_0)$ is always determined by the relationship $E_{\text{BOA}} = \int L_e(p_0, \Omega_0) \cdot \cos\theta_0 \, d\Omega_0$ where E_{BOA} is the bottom of atmosphere (BOA) irradiance of the light source. Compared to the commonly used strategy in which the light is emitted from the horizontal plane at the scene top as in (North, 1996; Thompson and Goel, 1998), this method is more robust, since it ensures that the scene can be fully illuminated along any light direction even with strong sloping topography.

Sunlight. If sunlight (solar direction Ω_s) is parallel, the direction PDF is interpreted as a Dirac delta function $p(\Omega_0) = \delta(\Omega_0 - \Omega_s)$. The emitted radiance is $L_e(p_0, \Omega_0) = \frac{E_{\text{BOA}}^{\text{dir}}}{\cos\theta_s} \cdot \delta(\Omega_0 - \Omega_s)$, where $E_{\text{BOA}}^{\text{dir}}$ is the direct irradiance at BOA. If the penumbra is simulated, the direction Ω_0 is uniformly sampled within solid angle $\Delta\Omega = \frac{A_{\text{sun}}}{(1\,AU)^2}$ (A_{sun} is the solar disk area, $1\,AU$ is the distance from the Earth to sun). Then, the emitted radiance is $L_e(p_0, \Omega_0) = \frac{E_{\text{BOA}}^{\text{dir}}}{\cos\theta_s \cdot \Delta\Omega}$.

Light from the sky. If it is isotropic, the direction PDF follows a cosine distribution $p(\Omega_0) = \frac{\cos\theta}{\pi}$. The emitted radiance is $L_e(p_0, \Omega_0) = \frac{E_{\text{BOA}}^{\text{diff}}}{\pi}$, where $E_{\text{BOA}}^{\text{diff}}$ is the diffuse irradiance at BOA. If it is anisotropic, the direction PDF and the emitted radiance is computed according to the energy distribution as described in (Wang and Gastellu-Etchegorry, 2021).

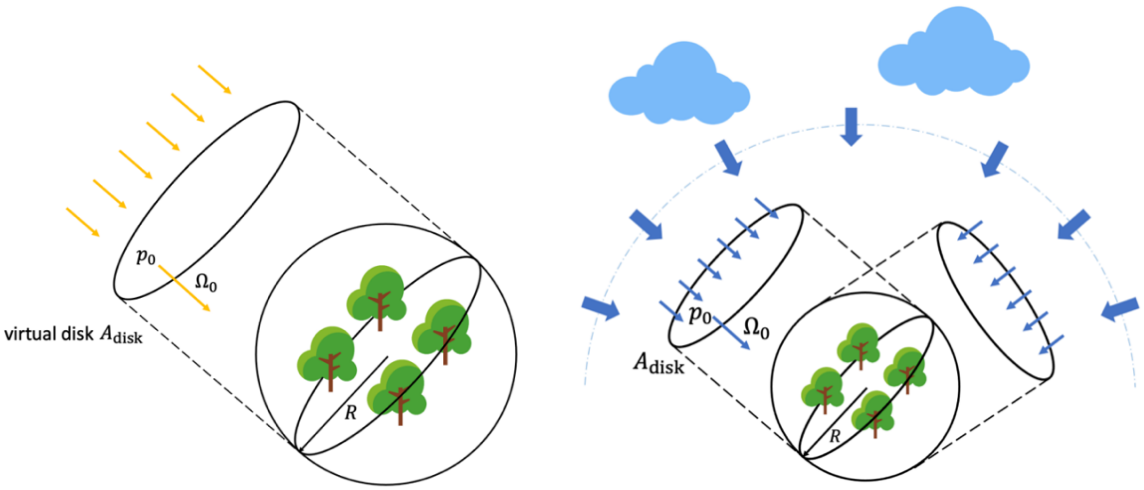

a) b)

Figure 7. Scene illumination of a) Parallel sunlight and b) diffuse light from the sky. The Earth scene is in a scene sphere with radius R. Sunlight or light from the sky originates from a virtual disk that is the projection of the scene sphere along the illumination direction.

3.4.2 Sensors

The two common remote sensing sensors, *i.e.*, pinhole camera and orthographic camera, are implemented. The pinhole camera has an infinitesimal lens. It is used to simulate airborne and in-situ observations with infinite depth of field. The orthographic camera has an infinitesimal field of view (FOV). It is used to simulate satellite images. For both cameras, the random walk starts by sampling a random vertex on the lens A_0 and a direction in the FOV. The computation of importance W_e is detailed in appendix A. In addition, a special camera, called BRF camera, is designed for an efficient simulation of the scene albedo, BRF and DBT.

Pinhole camera (Figure 3)**.** The pinhole is at a distance f in front of the image plane A_{img}. The vertex on the lens is sampled by a Dirac delta function $p(q_0) = \delta(q_0 - q_{\text{d}})$, with q_{d} the pinhole position. The direction is obtained by uniformly sampling a vertex q_{img} on the image plane and

connect q_0 on the lens. Since the lens does not refract rays, the directional PDF is derived from the relationship $p(\Omega_0)=p(q_{\text{img}})\cdot\frac{\left(\frac{f}{\cos\theta_i^{q_0}}\right)^2}{\cos\theta_i^{q_0}}=\frac{f^2}{A_{\text{img}}\cdot\cos^3\theta_i^{q_0}}$.

Orthographic camera (Figure 8)**.** It captures parallel radiation perpendicular to the image plane. Hence, the lens has the same shape as the image ($A_0 \equiv A_{\text{img}}$). The vertex on the lens is uniformly sampled with PDF $p(q_0)=\frac{1}{A_0}$ and the direction is sampled by a Dirac delta function $p(\Omega_0)=\delta(\Omega_0-\Omega_{\text{d}})$ with Ω_{d} the orientation of the camera.

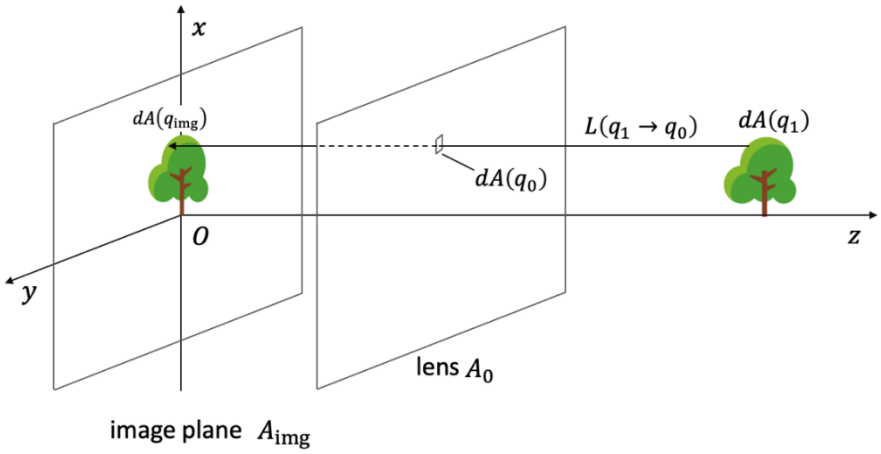

Figure 8. Orthographic camera. Lens with area A_0 is placed in front of the image plane A_{img} ($A_0 \equiv A_{\text{img}}$). Radiation from a differential surface $dA(q_1)$ in the scene along direction $q_1 \to q_0$ is focused by the lens onto the differential surface $dA(q_{\text{img}})$ at the image plane.

BRF camera. It is designed for BDPT algorithm to give the scene exit radiance. Its hemispheric image plane is an array of pixels that capture the scene upward radiation along a solid angle $\Delta\Omega=\int_{\Delta\varphi}\int_{\Delta\theta}\sin\theta\,d\theta d\varphi$ (Figure 9.b). Each pixel stores the scene average radiance along a direction $\Omega_0(\Delta\Omega)$. An exit direction is sampled with:

$$p(\Omega_0) = \frac{p(\theta,\varphi)}{\sin\theta}, \text{with } \begin{cases} p(\theta) = \dfrac{1}{\pi/2} \\ p(\varphi) = \dfrac{1}{2\pi} \end{cases} \quad (22)$$

Then, the vertex on the lens is uniformly sampled on the scene ortho-projected surface $A_{\text{ortho}}(\Omega_0)$ (Figure 9.a) along the viewing direction Ω_0 with PDF $p(q_0) = \frac{1}{A_{\text{ortho}}(\Omega_0)}$.

Compared to the photon spread method (Thompson and Goel, 1998) commonly implemented in forward light transport code, such as SPRINT and Rayspread, the BRF camera offers two advantages: (1) it is flexible to implement in Monte Carlo codes (*e.g.*, forward, backward and bi-directional light transport), and (2) the mean radiance/reflectance of any direction with any solid angle can be derived in a postprocess once the camera pixel values are computed.

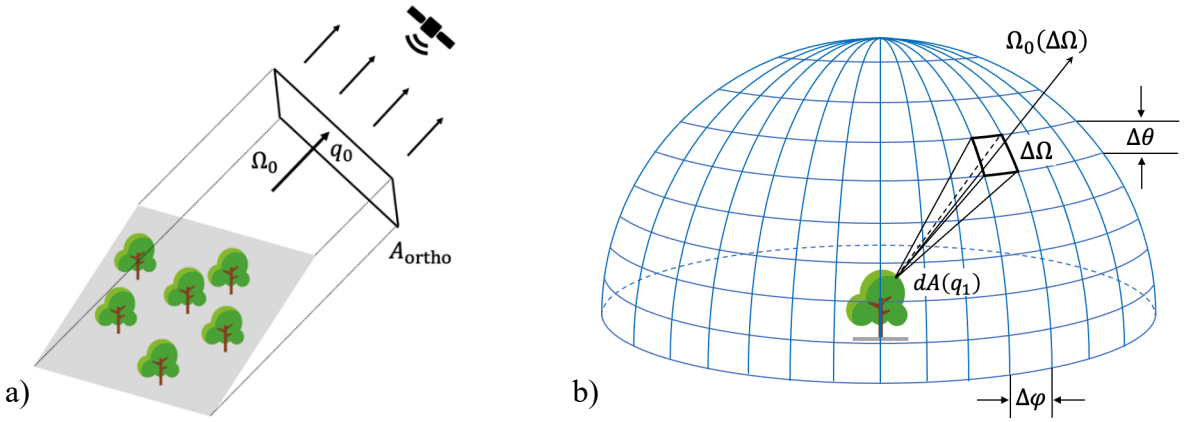

Figure 9. a) Exit radiation of a landscape along direction Ω_0 captured by a "specific" orthographic camera with image plane $A_{\text{ortho}}(\Omega_0)$. b) The hemispheric image plane of the BRF camera.

4 Comparison with standard DART-FT

Here, DART-Lux accuracy for BRF and remote sensing images is assessed using DART-FT as a reference. Indeed, as indicated in section 2.2, DART-FT accuracy is ~0.02 for reflectance, <

2 K for brightness temperature and ~1% compared to benchmark RT models. Three scenes are considered: schematic scene, urban scene and forest scene.

4.1 Schematic scene

The schematic scene (Figure 10) has seven cherry trees with different sizes and a DART-created house with gable roof to assess DART-Lux accuracy in presence of slopes. Its mock-up consists of 0.137 million facets. Table 1 and Table 2 give DART input parameters. Its BOA images are simulated for four spectral bands (blue B: 0.44 μm; green G: 0.56 μm; red R: 0.66 μm; near infrared NIR: 0.87 μm) at 0.125m spatial resolution, for three light conditions (*i.e.*, single and multiple light sources) with SKYL $= \frac{\text{BOA sky diffuse irradiance}}{\text{BOA total irradiance}}$ equal to 0 (direct sun), 1 (diffuse sky) and 0.5 (direct sun + diffuse sky).

Table 1. Input parameters for the mock-up, light source and spectral band.

Parameters		**Value**
DART scene	Scene dimension	$X = Y = 32$ m
	Spatial resolution	$\Delta x = \Delta y = 0.125$ m
	Tree model	Cherry tree
	Building model	DART classic house
	Neighborhood effect	Repetitive mode
Sunlight	Direction	Zenith angle $\theta_{sun} = 30°$, Azimuth angle $\varphi_{sun} = 225°$
	TOA irradiance	THKUR (Berk et al., 2008)
Sky light	SKYL	0, 0.5 or 1
Spectral band	Spectral band	0.44 μm, 0.56 μm, 0.66 μm, 0.87 μm
	Bandwidth	0.02 μm

Table 2. Configurations of DART-Lux and DART-FT RT methods.

DART-Lux		DART-FT	
Samples/pixel	400	Discrete direction	1000
Max scattering order	6	Max scattering order	6
Number of threads	8	Number of threads	8
		Illumination rays per pixel	169

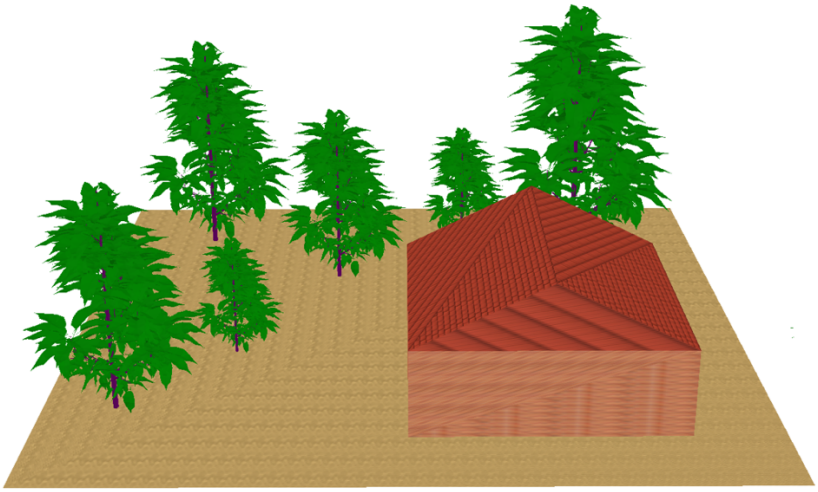

Figure 10. Mock-up of the schematic scene: 7 cherry trees of different sizes and a DART classic house.

The consistency of DART-Lux and DART-FT images is illustrated by the visual comparison of their RGB colour composite images (Figure 11) and by the scatter plots of their NIR reflectance (Figure 12) for the three BOA illumination conditions. Degrading the image resolution from 0.125m to 0.5 m greatly improves the pixelwise comparison from $\{R^2 > 0.968$, bias $< 0.006\}$ to $\{R^2 > 0.995$, bias $< 0.0004\}$ because it mitigates the noise and discretization effects. Figure 13 shows the BRF profiles in the solar plane for the four spectral bands (B, G, R, NIR), with viewing zenith angle step $\Delta\theta_v = 5°$. Differences are quantified by the average

absolute relative difference $\bar{\varepsilon} = \frac{1}{N_{\theta_v}} \sum_{\theta_v} \left| \frac{\rho_{\text{DART-LUX}}(\theta_v) - \rho_{\text{DART-FT}}(\theta_v)}{\rho_{\text{DART-FT}}(\theta_v)} \right| \cdot 100\%$ with N_{θ_v} the number of viewing directions. Usually, $\bar{\varepsilon}$ ≈0.4% (Table 3) and maximal $\bar{\varepsilon}_{\max}$ ≈ 0.6%. The slight differences in the scatter plot and the BRF profile are mostly due to DART-Lux Monte Carlo noise and DART-FT discretization processes. Indeed, even with 1000 discrete directions, the DART-FT "atmosphere shadows" (*i.e.*, SKYL = 1) have a discrete aspect less realistic than that with DART-Lux.

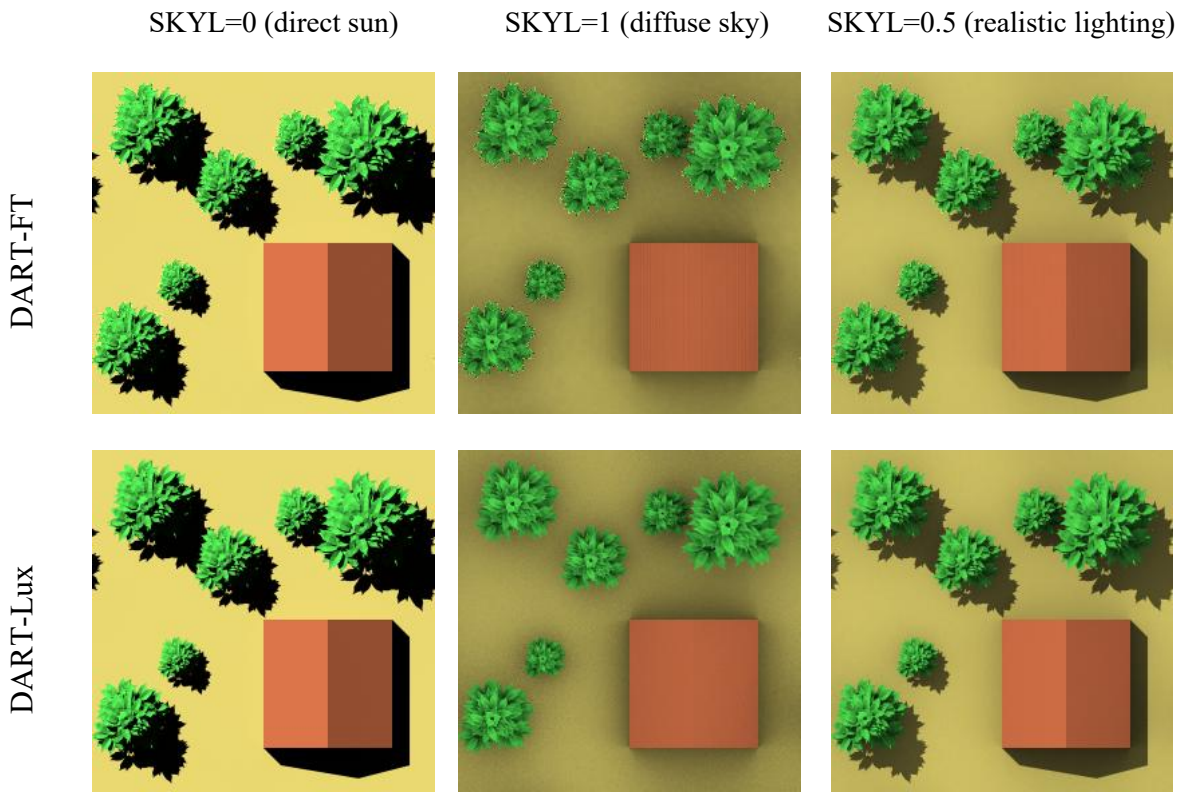

Figure 11. DART-FT (top) and DART-Lux (bottom) RGB images for three light conditions: SKYL=0 (left), SKYL=1 (centre) and SKYL=0.5 (right).

SKYL = 0 SKYL = 1 SKYL = 0.5

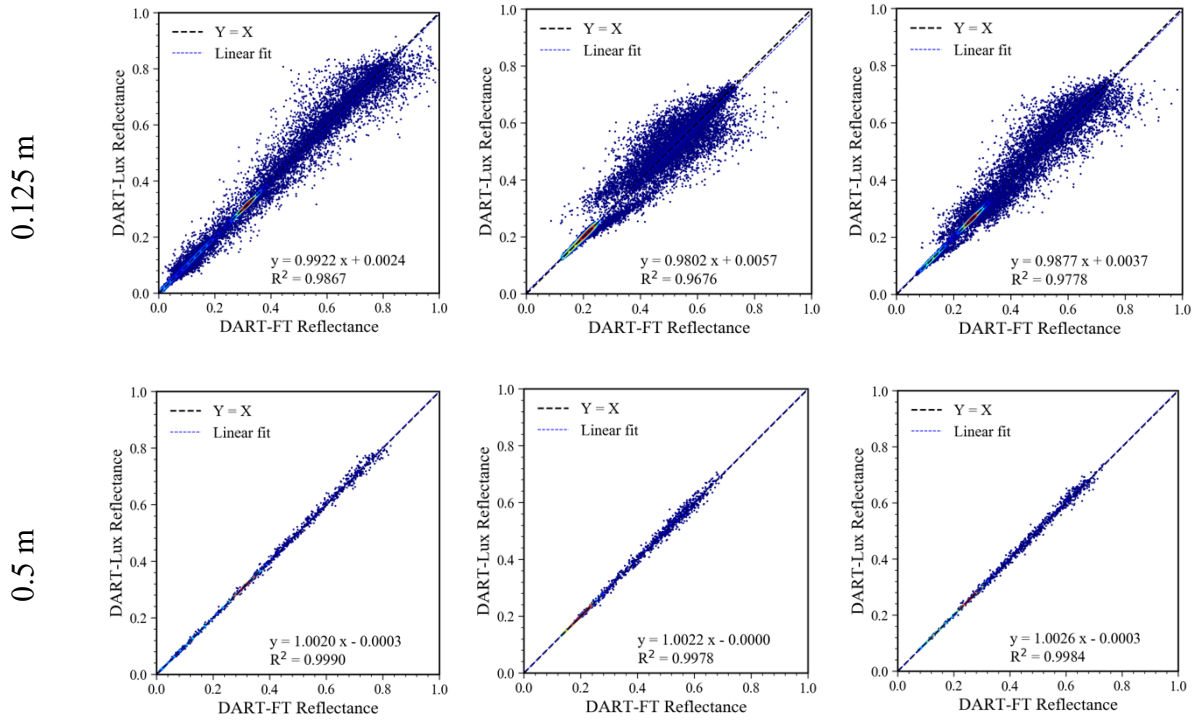

479 Figure 12. Pixelwise comparison of DART-FT and DART-Lux NIR reflectance. Pixel values
480 at 0.5 m resolution result of the degradation of the initial image at 0.125 m resolution.

481

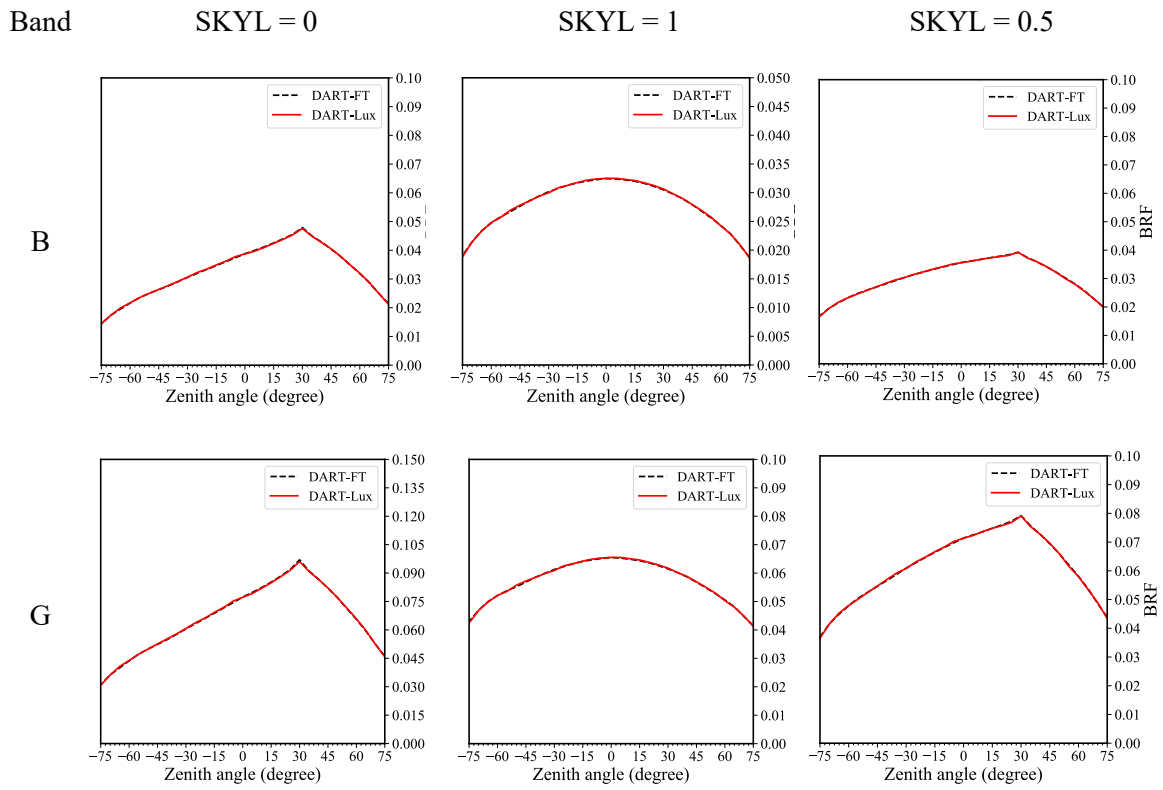

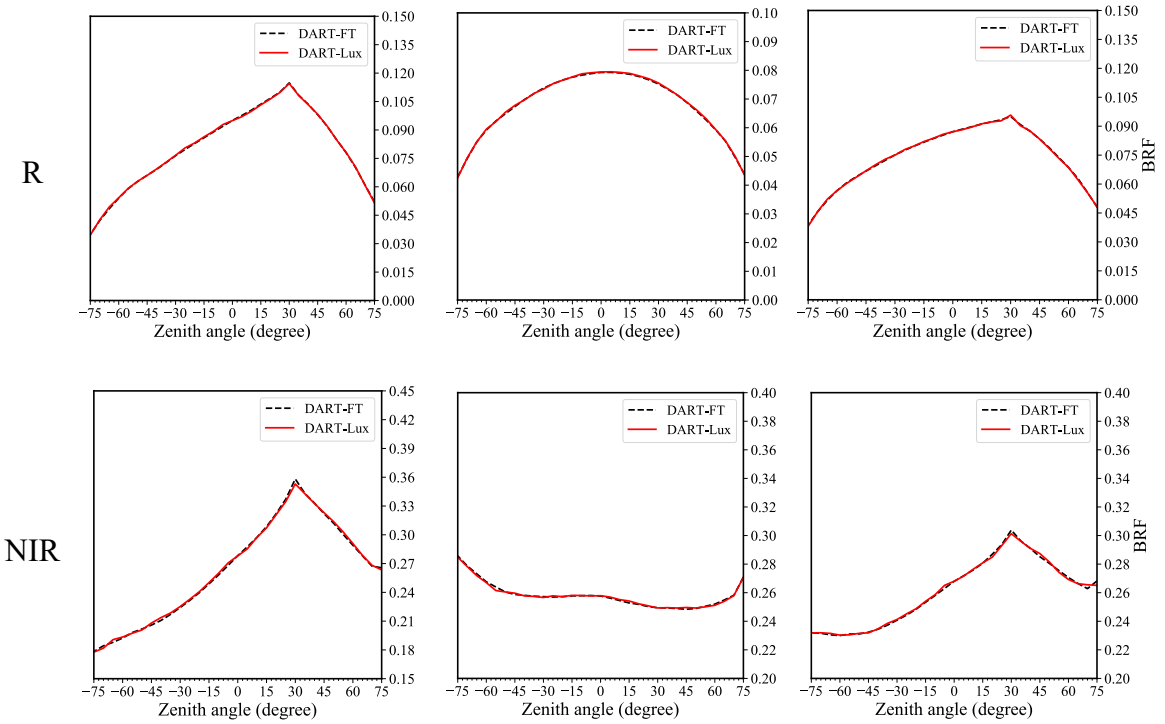

Figure 13. DART-FT and DART-Lux solar plane reflectance ($\Delta\theta_v = 5°$) in four spectral bands (R, G, B, NIR) for three illuminations (SKYL=0, SKYL=1, SKYL=0.5).

Table 3. Summary of average absolute relative difference $\bar{\varepsilon}$ of BRF in Figure 13.

Band	SKYL = 0	SKYL = 1	SKYL = 0.5
B	0.443	0.335	0.360
G	0.467	0.336	0.359
R	0.445	0.349	0.404
NIR	0.605	0.226	0.338

4.2 Urban scene

The urban scene is the Brienne district (1400 m × 750 m) of Toulouse, France. Its 3D mock-up (Figure 14.a) was provided by the Toulouse townhall. It contains 953 buildings, 2433 trees, 3 grasslands, 1 river, 1 canal and other city facilities, represented by 8 million facets. DART-FT and DART-Lux are configured with direct sun light ($\theta_{\text{sun}} = 20°, \varphi_{\text{sun}} = 180°, \text{SKYL} = 0$),

0.5 m spatial resolution, four spectral bands (B: 0.44 μm, G: 0.55 μm, R: 0.66 μm, NIR: 0.87 μm), maximal scattering orders 6, no topography, and no atmosphere. Common optical properties are assigned per type of urban element (e.g., roof, vegetation). DART-FT is run with 100 discrete directions and 100 illumination rays per pixel. DART-Lux is run with 60 samples per pixel.

DART-FT and DART-Lux RGB images are very close as illustrated by their RGB colour composites (Figure 14) and scatter plot of pixel reflectance in R band at 0.5m resolution (Figure 15.a): R^2>0.99 and bias ~0.0001. Degrading image resolution down to 2.0 m improves their similarity: R^2>0.999 and bias <0.0001 (Figure 15.b). Figure 15.c shows the R band BRF in the solar plane with zenith angle step $\Delta\theta_v = 2°$. Its average absolute relative difference $\bar{\varepsilon}$ is 0.24%.

a)

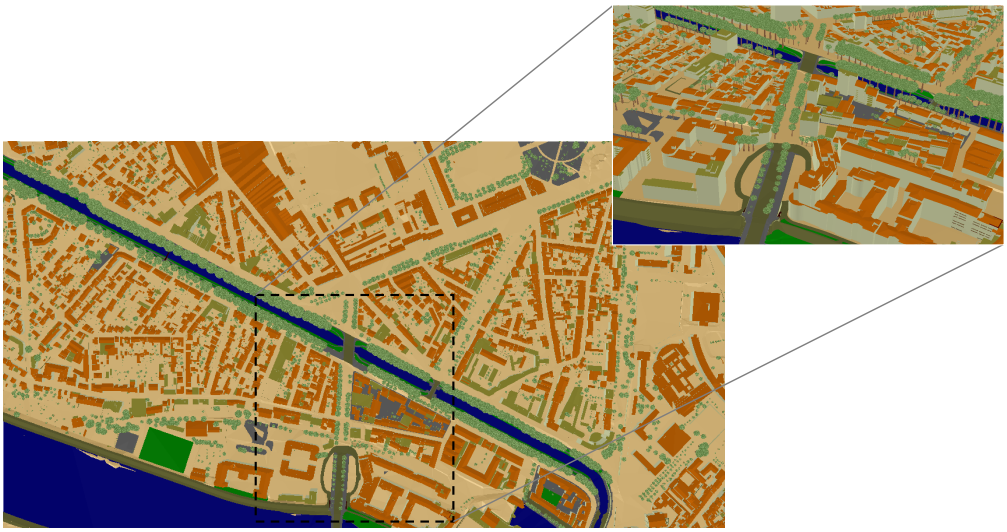

b)

c)

503 Figure 14. Brienne district: 3D mock-up (1400 m × 750 m) (a) and its DART-FT (b) and DART-Lux

504 (c) RGB images.

505

a)

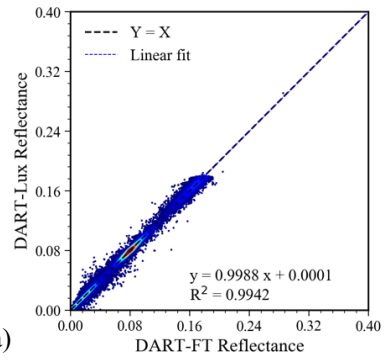

b)

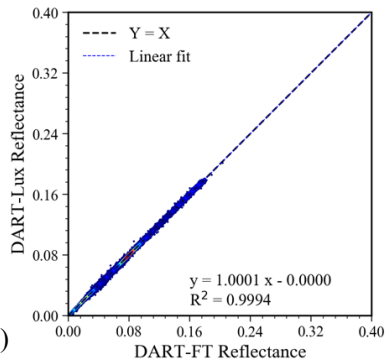

c)

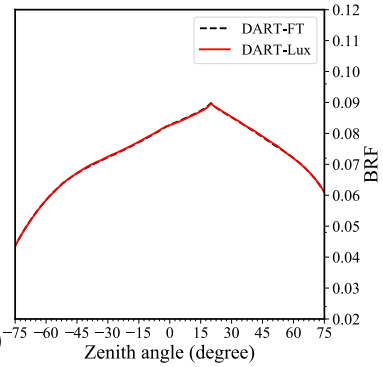

Figure 15. DART-Lux and DART-FT reflectance in R band. Scatter plot of pixel reflectance for 0.5 m (a) and 2.0 m (b) spatial resolution. c) Reflectance in the solar plane.

4.3 Forest scene

The forest scene is the Järvselja summer birch forest (summer, HET09_JBS_SUM) of RAMI4 experiment (https://rami-benchmark.jrc.ec.europa.eu). It has 1029 realistic trees with 465 birch trees, 196 common alder trees, 185 aspen trees, 78 linden trees, 39 spruce trees, and 46 ash and maple trees (Figure 16). Its mock-up is created by repeating and/or rotating 18 individual 3D tree objects. For example, the 465 birch trees are generated by cloning and/or rotating 4 birch tree objects at different growing stages. This forest stand is very challenging for 3D RT models (Figure 3 in (Widlowski et al., 2015)) because it consists of more than 550 million facets.

Simulations are for direct sun illumination ($\theta_{\text{sun}} = 36.6°, \varphi_{\text{sun}} = 270.69°$, SKYL=0), 0.125 m spatial resolution, 4 spectral bands (B: 0.44 μm, G: 0.55 μm, R: 0.66 μm, NIR: 0.87 μm), maximal scattering order 6, and specific optical properties are assigned per tree species. DART-Lux is run with 200 samples per pixel. DART-FT is run with 62500 illumination rays per pixel, and 80 discrete directions. Figure 16.b shows DART-FT and DART-Lux RGB color composite images. As for the schematic and urban cases, the scatter plots of pixel NIR reflectance indicate that the pixelwise comparison greatly improves from 0.125 m spatial resolution (Figure 16.d): $\{R^2 > 0.93, \text{bias} \approx 0.01\}$ to 1 m spatial resolution (Figure 16.e): $\{R^2 > 0.997, \text{bias} < 0.002\}$.

Figure 16.f shows DART-FT and DART-Lux NIR reflectance in the solar plane, at first order scattering. DART-FT is run with and without an acceleration technique: rays that exit a cell face along a same direction are not merged (approximate case called DART-FT) or merged (accurate case called DART-FT-REF, used as a reference). DART-Lux average absolute

relative difference is $\bar{\varepsilon} = 0.5\%$ for DART-FT-REF and 0.7% for DART-FT. Larger differences occur at the hot spot direction. DART-FT underestimates the hot spot (Figure 16.f) because its merging technique reduces the exactly backscattered rays. Multiple scattering is only simulated with DART-FT and DART-Lux because DART-FT-REF is very time and memory consuming. The average absolute difference $\bar{\varepsilon}$ between DART-Lux and DART-FT is 1.0% (Figure 16.g).

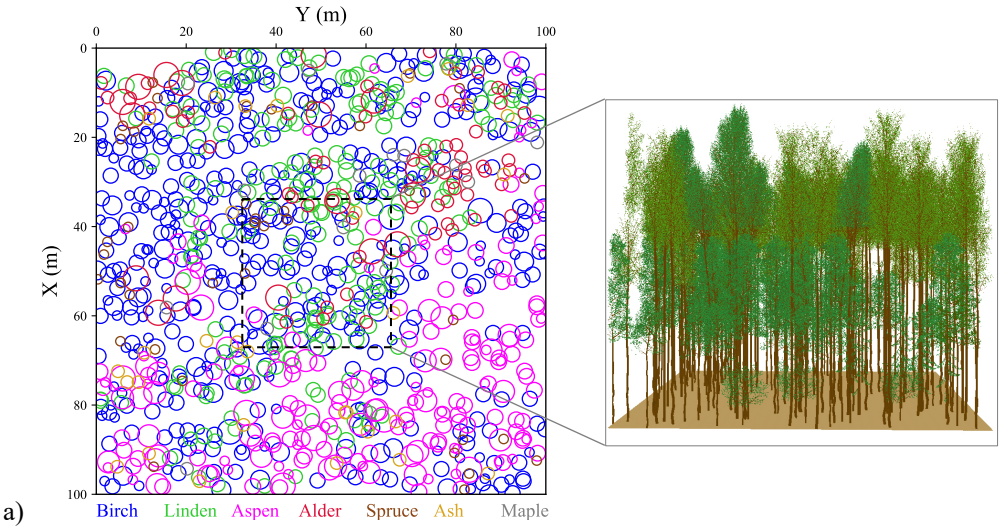

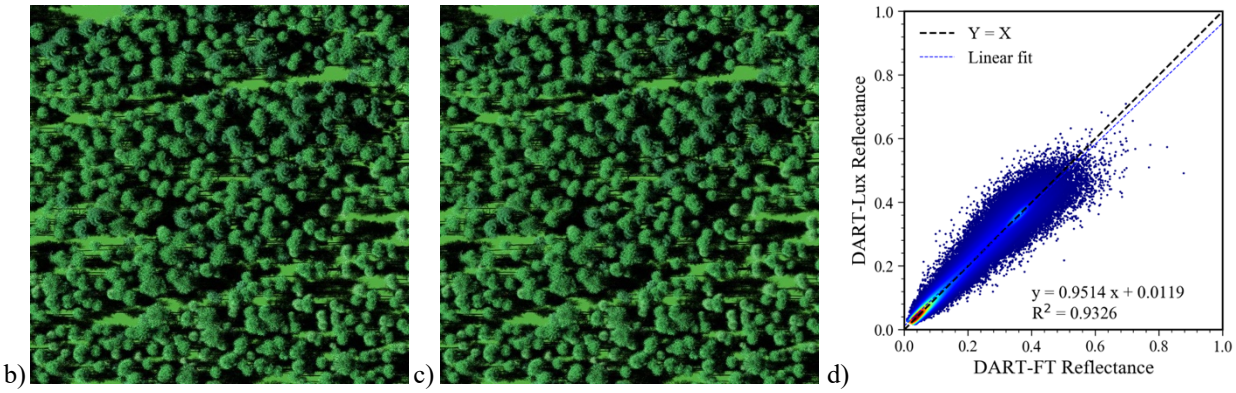

g)

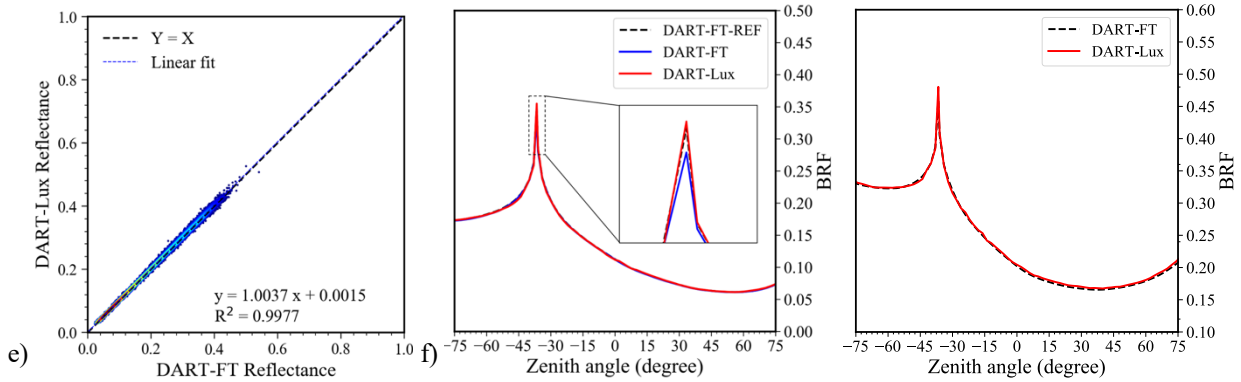

Figure 16. Järvselja birch forest. a) Location of trees and 3D mock-up of the centre region. DART-FT (b) and DART-Lux (c) RGB images at resolution 0.125 m. Scatter plot of pixel NIR reflectance at resolution 0.125 m (d) and 1.0 m (e). DART-FT and DART-Lux NIR reflectance in the solar plane with zenith angle step $\Delta\theta_v = 2°$: f) single scattering reflectance, g) total reflectance.

5 Discussion

5.1 Correlation of path samples

The BDPT (*cf.* section 3.2) with N_v vertices per random walk is very efficient because it creates N_v^2 paths with only $N_v^2 + 2(N_v - 1)$ intersection tests, compared to N_v^3 if each path is created independently. Knowing that the intersection test is the most computational expensive process in 3D RT modelling, the BDPT decreases simulation time by a factor $\frac{N_v^3}{N_v^2+2(N_v-1)}$. However, it increases the covariance (*i.e.*, Monte Carlo noise) between path samples, because they are created with the same light and sensor sub-paths. Although the MIS estimator gives unbiased results (*cf.* appendix D), compared to estimates with independent path samples, the path sample correlation can increase the overall variance by a maximal factor *f*. With $\tau \approx \frac{C_{\mathcal{D}n}}{C_{\mathcal{D}n+1}}$ $(0 \leq \tau < 1)$ the average ratio of contributions of successive scattering orders (*cf.* appendix E), we have:

$$f(\tau) = \frac{(1+\tau)\cdot\left(2+\tau\left(\frac{\sqrt{2}}{2}-\tau\right)(3-\tau)\right)}{(1-\tau)^2} \tag{23}$$

Figure 17.a shows the decrease in the contribution of the scene radiance of scattering order $n = 1$ to 6, relative to the contribution of first order scattering, for the three scenes studied in section 4. The trendiness is an exponentiation $g(n)=\tau^{-(n-1)}$ with τ that in [0, 0.1] for most simulations in visible bands and in [0.4, 0.6] for most simulations in the NIR band. $f(\tau)$ of Eq. (23) (Figure

17.b) is less than 2.4 for simulations in visible bands, and in [9, 22] for most simulations in the NIR band, which stresses that DART-Lux usually converges faster in visible bands than in NIR bands. This is also underlined by the BRF profiles (Figure 13): results are noisier in NIR bands than in visible bands if the same number of samples per pixel is used.

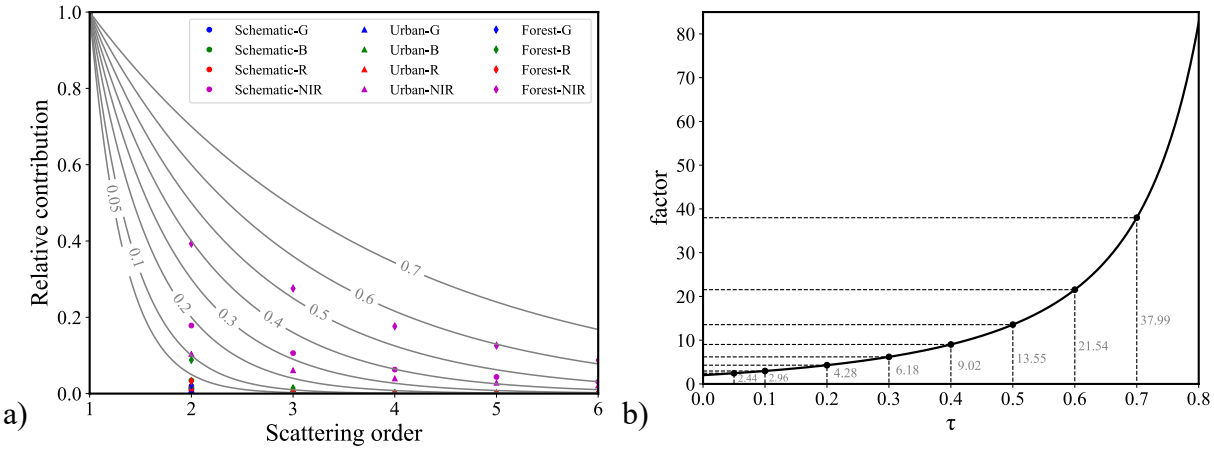

Figure 17. Contribution $g(n)$ of scene radiance for scattering order n = 1 to 6, relative to the contribution of first order scattering, for the three studied scenes: schematic, urban and forest. a) Trendlines $g(n)=\tau^{-(n-1)}$. b) Factor f in function of τ value (Eq. (23)).

The efficiency η of a Monte Carlo method depends on its variance $\mathbb{V}$ and computation time $\mathbb{T}$ (Eq. (24)) (Veach, 1997).

$$\eta = \frac{1}{\mathbb{V} \cdot \mathbb{T}} \tag{24}$$

Compared to the use of independent paths, the DART-Lux BDPT algorithm appears to be more efficient despite the correlation of its path samples. The efficiency gains of DART-Lux over the method with independent path samples is $\gamma = \left(\frac{\eta_{\text{DART-Lux}}}{\eta_{\text{independent path}}} - 1\right) = \left(\frac{1}{f} \cdot \frac{{N_v}^3}{{N_v}^2+2(N_v-1)} - 1\right)$. In visible bands, usually $N_v = 5$, $f \leq 2.5$, then $\gamma > 50\%$. In NIR bands, usually $N_v \geq 40$, $f \leq 22$, then $\gamma > 70\%$. Actually, γ is even larger because the variance is usually smaller than the upper boundary variance.

5.2 Advantages of DART-Lux for simulating images

Compared to DART-FT, DART-Lux has great advantages for simulating remote sensing images and BRF, especially for complex scenes with millions of facets. Table 4 summarizes the memory demand and computation time of simulations in section 4. For the Järvselja birch forest, DART-Lux reduces the simulation time by 715 times, and the memory by 142 times. Four factors explain DART-Lux efficiency. 1) End-to-end simulation: DART-Lux samples the paths that contribute only to the simulated image whereas DART-FT tracks all possible paths. 2) Efficient path generating strategy: bi-directional random walk and vertex connection ways can generate a group of paths with less time cost. Despite the potential increase of variance since path samples can be correlated, the overall efficiency increases (*cf.* section 5.1). 3) Depth-first strategy: the random walk requires much less memory compared to the breadth-first strategy of DART-FT whose memory demand greatly increases with scattering order. Although DART-FT applies an acceleration technique by merging rays that come out of a cell face for each discrete direction (*cf.* section 4.3), its memory usage is still very high for modelling large-scale landscapes. 4) Data organisation: for a scene with N instances of a 3D object, DART-Lux cloning technique stores a unique 3D object and N rotation – scaling matrices whereas DART-FT stores N 3D objects in the memory for simulating the 3D radiative budget. Therefore, DART-Lux uses much less memory and time than DART-FT.

Table 4. Simulation time and memory demand for the three cases of section 4. Cases 1 and 2 are simulated on a personal computer (Intel Xeon E5-1620 @ 3.5 GHz, 8 cores, 64 Gb memory). Case 3 is simulated on a server (Intel Xeon E5-2687W @ 3.1 GHz, 40 cores, 560 Gb memory).

Scene	DART-FT		DART-Lux	
	Time (min)	Memory (Gb)	Time (min)	Memory (Gb)

Case 1: Schematic	70.8	1.25	1.38	0.07
Case 2: Urban	571	40.0	10.86	2.60
Case 3: Forest	4962	469.0	6.93	3.30

597

598 **5.3 Accuracy of DART-Lux**

599 In theory, the Monte Carlo method is more accurate than the discrete ordinates method, because
600 it does not need mock-up or modelling simplifications. The DART-FT underestimation of the
601 hot-spot in Figure 16.f illustrates this point. However, because Monte Carlo methods need many
602 samples to reach convergence, there is a trade-off between accuracy and number of samples.
603 Fortunately, DART-Lux accuracy and efficiency is less dependent than DART-FT on the scene
604 complexity. For example, the forest scene has an average computation time per sample (*i.e.*,
605 $\frac{\text{Simulation time}}{\text{Number of samples}}$) that is only 7 times longer than for the schematic scene, whereas it is 4000
606 times more complex than the schematic scene in terms of number of facets (Table 5). Table 6
607 shows the accuracy of DART-Lux forest reflectance for six values of samples/m^2: difference
608 $\varepsilon_{\text{mean}}$ of image mean reflectance, and RMSE $\varepsilon_{\text{pixel}}$ of image pixel reflectance relative to the
609 reference values computed with a huge number of samples/m^2. Results stress that DART-Lux
610 configuration can be optimized according to the application and accuracy requirements. 1)
611 Convergence is much faster for low reflectance bands than high reflectance bands, which is
612 consistent with discussion in section 5.1. 2) $\varepsilon_{\text{mean}}$ and $\varepsilon_{\text{pixel}}$ decrease with the increase of
613 samples/m^2, with a much faster convergence for $\varepsilon_{\text{mean}}$ than for $\varepsilon_{\text{pixel}}$.

614

615 Table 5. Average time cost per sample $\frac{\text{Simulation time}}{\text{Number of samples}}$ of the schematic and forest scenes in section
616 4, for an Intel Xeon E5-2687W server (3.1 GHz, 40 cores, 560 Gb memory).

Scene	Nb facet	Nb pixels	Samples/pixel	Time (min)	Time/sample (μs)

Case 1: Schematic	0.137 10^6	65536	400	0.20	**0.45**
Case 3: Forest	558.2 10^6	640000	200	6.93	**3.25**

Table 6. Absolute nadir reflectance error $\varepsilon_{\text{mean}}$ and pixel RMSE $\varepsilon_{\text{pixel}}$ of forest scene in the G and NIR bands for six samples/m^2 values; reference images are simulated with 128000 samples/m^2.

	Samples/m^2	**640**	**3200**	**6400**	**12800**	**25600**	**51200**
G	$\varepsilon_{\text{mean}}$	3.8E-6	9.7E-6	4.0E-7	2.4E-6	1.5E-6	2.1E-6
	$\varepsilon_{\text{pixel}}$	0.010	0.005	0.003	0.002	0.002	0.001
NIR	$\varepsilon_{\text{mean}}$	3.0E-6	4.1E-5	1.2E-5	4.9E-6	1.3E-5	1.1E-5
	$\varepsilon_{\text{pixel}}$	0.075	0.034	0.024	0.018	0.013	0.010

6 Conclusion and perspectives

The unbiased, rapid and robust DART-Lux is a new Monte Carlo RT method in DART. Its physical modelling relies on a bidirectional path tracing algorithm that efficiently samples a group of paths between the light source and the sensor to estimate radiance measurements. The algorithm is flexible to incorporate multi light sources (*e.g.*, sun and sky) and multi sensors (perspective camera, orthographic camera, BRF camera). It greatly improves the computational efficiency of DART to simulate spectral images and BRF. Its accuracy and efficiency are assessed by standard DART-FT for three landscapes (*i.e.*, schematic scene, urban scene, forest scene). Compared to DART-FT, DART-Lux gives consistent results (relative difference < 1%) while reducing the computation time by up to a factor of 700. In addition, conversely to DART-FT, its accuracy and efficiency depend much less on the landscape complexity.

A theoretical demonstration gives analytical expressions of the computation time and the largest variance. It appears that DART-Lux algorithm improves efficiency η (*i.e.*, inverse of Variance

× Computation time) even if it creates correlated path samples. It also has great advantages and is much faster for simulating remote sensing images due to end-to-end modelling, efficient path sampling and depth-first strategy. Finally, a sensitivity study shows that DART-Lux error decreases with the number of samples, image mean values converges much faster than image pixel values, and the convergence is faster for low reflectance bands than for high reflectance bands.

The high-performance DART-Lux addresses the requirements for simulating large-scale and complex landscapes and massive remote sensing data, as well as the trends in RT model development. The Monte Carlo approach is potentially better adapted than discrete ordinates method for designing and implementing complex physical phenomena such as adjacency effects and clouds scattering and shadowing. DART-Lux opens new avenues for many remote sensing applications: design of satellite missions; correction of directional effects; inversion of remote sensing images; training machine learning models with a large amount of images; studying the impact of complex 3D architecture, *etc*. DART-Lux modelling development is still underway to expand DART functionality, including SIF and thermal emission, LiDAR, atmospheric RT, polarization and 3D radiative budget (Gastellu-Etchegorry et al., 2022; Regaieg et al., 2022; Yang et al., 2022).

Acknowledgement

This work is funded by Région Occitanie Pyrénées-Méditerranée, France and TOSCA program of CNES. We are grateful to CNRS for funding the PhD of Omar Regaieg through the 80|Prime program and to Dr I. Georgiev (Saarland University, German) and W. Huang (Walt Disney Animation Studio, USA) for their advice on the algorithm of bidirectional path tracing. We also

659 thank Toulouse Metropole, and in particular M. Pagès, Head of the Digital Land Modelling
660 Service, for providing the urban geometric database of the district of Toulouse used in this work.
661

Appendix A. Definition of the importance function

The importance function $W_e(r_0, \Omega_0)$ (Nicodemus, 1978), quantifies the sensor response $dS(r_0, \Omega_0)$ to the flux $d\Phi(r_0, \Omega_0)$ incident on the sensor lens at r_0 along direction Ω_0.

$$dS(r_0, \Omega_0) = W_e(r_0, \Omega_0) d\Phi(r_0, \Omega_0) \quad \text{(A.1)}$$

With the usual assumption of constant W_e for a position r_0 and a direction Ω_0, the sensor response of pixel j is:

$$\mathrm{S}^{(j)} = \int_{A_0} \int_{\Delta\Omega_0} {W_e}^{(j)}(r_0, \Omega_0) d\Phi(r_0, \Omega_0) = \int_{A_0} \int_{\Delta\Omega_0} {W_e}^{(j)}(r_0, \Omega_0) \cdot L(r_1 \rightarrow r_0) \cos\theta_i^{r_0} \, d\Omega_0 dA(r_0) \quad \text{(A.2)}$$

DART-Lux importance function $W_e(r_0, \Omega_0)$ is such that it transfers the sensor response $\mathrm{S}^{(j)}$ to radiance measurement $L^{(j)}$ (*i.e.*, average radiance for pixel area $A_{\mathrm{img}}^{(j)}$), knowing $L(r_{\mathrm{img}})$ at r_{img}:

$$L^{(j)} = \frac{1}{A_{\mathrm{img}}^{(j)}} \int_{A_{\mathrm{img}}^{(j)}} L(r_{\mathrm{img}}) dA(r_{\mathrm{img}}) \quad \text{(A.3)}$$

Below, we give the expression of $W_e(r_0, \Omega_0)$ for two sensors:

<u>*Pinhole camera*</u> ($A_0 \ll A_{\mathrm{img}}$, Figure 3): the optical system does not refract incident rays. Eq.(A.3) gives $L^{(j)} = \frac{1}{A_{\mathrm{img}}^{(j)}} \cdot \int_{\Delta\Omega_0^{(j)}} L(r_1 \rightarrow r_0) \cdot J_{\mathrm{T}} d\Omega_0$ with transfer function $J_{\mathrm{T}} = \frac{(f/\cos\theta_i^{r_0})^2}{\cos\theta_i^{r_0}}$ and solid angle $\Delta\Omega_0^{(j)}$ that contains the directions that are mapped to $A_{\mathrm{img}}^{(j)}$. Comparing $L^{(j)}$ to Eq. (A.2) and assuming that $\int_{\Delta\Omega_0} {W_e}^{(j)}(r_0, \Omega_0) \cdot L(r_1 \rightarrow r_0) \cdot \cos\theta_i^{r_0} \, d\Omega_0$ is constant over A_0, we have:

$${W_e}^{(j)}(r_0, \Omega_0) = \begin{cases} \dfrac{f^2}{A_{\mathrm{img}}^{(j)} \cdot A_0 \cdot \left(\cos\theta_i^{r_0}\right)^4}, & \Omega_0 \in \Delta\Omega_0^{(j)} \\ 0, & \Omega_0 \notin \Delta\Omega_0^{(j)} \end{cases} \quad \text{(A.4)}$$

<u>*Orthographic camera*</u> ($A_0 \equiv A_{\mathrm{img}}$, Figure 8): it captures light in very narrow $\Delta\Omega_0$. With Ω_{d} the camera orientation, $\mathrm{S}^{(j)} = \int_{A_0} \frac{{W_e}^{(j)}(r_0, \Omega_0)}{\delta(\Omega_0 - \Omega_{\mathrm{d}})} \cdot L(r_1 \rightarrow r_0) dA(r_0)$. Its comparison to Eq. (A.3) gives:

$${W_e}^{(j)}(r_0, \Omega_0) = \frac{\delta(\Omega_0 - \Omega_{\mathrm{d}})}{A_{\mathrm{img}}^{(j)}} \quad \text{(A.5)}$$

Appendix B. Importance transport equation (backward light transport)

Christensen et al. (1993) proved that the backward and forward light transport are symmetric if the BSDF reciprocity is verified. Then, the importance function W_e can be treated equivalently as an exit quantity as the emitted radiance L_e. The importance function $W^{(j)}(r \to r')$ along direction $r \to r'$ quantifies the contribution of the exit radiance at r' to the radiance measurement at pixel j. Let a virtual ray carrying $W^{(j)}(r \to r')$ that starts from r, and is virtually scattered to r'' after being intercepted at r'. The adjoint formulation of Eq. (3) is:

$$W^{(j)}(r' \to r'') = W_e{}^{(j)}(r' \to r'') + \int_A W^{(j)}(r \to r') \cdot f(r \to r' \to r'') \cdot G(r \leftrightarrow r') dA(r) \qquad \text{(B.1)}$$

Eq. (3) and Eq. (B.1) are symmetric if there is BSDF reciprocity, *i.e.*, $f(r \to r' \to r'') = f(r'' \to r' \to r)$.

Appendix C. MIS weight evaluation

Direct evaluation of the MIS weight is very computationally expensive, which reduces the efficiency of the bidirectional path tracing algorithm. DART-Lux uses an efficient method to evaluate it incrementally along the random walk.

The power heuristic MIS weight is:

$$w_{s,t}(\bar{r}_{s,t}) = \frac{\left(p(\bar{r}_{s,t})\right)^2}{\sum_{s'=0}^{n+1}\left(p(\bar{r}_{s',t'})\right)^2} \tag{C.1}$$

where $s+t = s'+t' = n+1$. The virtual path $\bar{r}_{s',t'}$ with $(s',t') \neq (s,t)$ has the same vertices as the sampled path $\bar{r}_{s,t}$, but is generated with another sampling way (Figure 6). The term "virtual path" emphasizes that the path is only used to evaluate the MIS weight $w_{s,t}(\bar{r}_{s,t})$.

The division of Eq. (C.1) by $\left(p(\bar{r}_{s,t})\right)^2$ gives:

$$w_{s,t}(\bar{r}_{s,t}) = \frac{1}{w_{s-1}^{\text{light}} + 1 + w_{t-1}^{\text{sensor}}} \tag{C.2}$$

with

$$w_{s-1}^{\text{light}} = \sum_{s'=0}^{s-1}\left(\frac{p(\bar{r}_{s',t'})}{p(\bar{r}_{s,t})}\right)^2 \text{ and } w_{t-1}^{\text{sensor}} = \sum_{t'=0}^{t-1}\left(\frac{p(\bar{r}_{s',t'})}{p(\bar{r}_{s,t})}\right)^2 \tag{C.3}$$

The terms $\vec{p}(p_k) \equiv p(p_k|p_{k-1},p_{k-2})$, $\overleftarrow{p}(p_k) \equiv p(p_k|p_{k+1},p_{k+2})$ and $\vec{p}(q_k) \equiv p(q_k|q_{k+1},q_{k+2})$, $\overleftarrow{p}(q_k) \equiv p(q_k|q_{k-1},q_{k-2})$ are used to simplify the expressions of $p(\bar{r}_{s,t})$ and $p(\bar{r}_{s',t'})$:

$$p(\bar{r}_{s,t}) = p(\bar{p}_s)\cdot p(\bar{p}_t) = \prod_{k=0}^{s-1}\vec{p}(p_k)\cdot\prod_{k=0}^{t-1}\overleftarrow{p}(q_k) \tag{C.4}$$

$$p(\bar{r}_{s',t'}) = \begin{cases} \prod_{k=0}^{s'-1} \vec{p}(p_k) \cdot \prod_{k=s'}^{s-1} \overleftarrow{p}(p_k) \cdot \prod_{k=0}^{t-1} \overleftarrow{p}(q_k), s' < s \\ \prod_{k=0}^{s-1} \vec{p}(p_k) \cdot \prod_{k=t'}^{t-1} \vec{p}(q_k) \cdot \prod_{k=0}^{t'-1} \overleftarrow{p}(q_k), s' > s \end{cases}$$

Using Eq. (C.4), Eq. (C.3) can be expanded as

$$\begin{aligned} w_{s-1}^{\text{light}} &= \sum_{s'=0}^{s-1} \left(\frac{\prod_{k=0}^{s'-1} \vec{p}(p_k) \cdot \prod_{k=s'}^{s-1} \overleftarrow{p}(p_k) \cdot \prod_{k=0}^{t-1} \overleftarrow{p}(q_k)}{\prod_{k=0}^{s-1} \vec{p}(p_k) \cdot \prod_{k=0}^{t-1} \overleftarrow{p}(q_k)} \right)^2 = \sum_{s'=0}^{s-1} \left(\prod_{k=s'}^{s-1} \frac{\overleftarrow{p}(p_k)}{\vec{p}(p_k)} \right)^2 \\ w_{t-1}^{\text{sensor}} &= \sum_{t'=0}^{t-1} \left(\frac{\prod_{k=0}^{s-1} \vec{p}(p_k) \cdot \prod_{k=t'}^{t-1} \vec{p}(q_k) \cdot \prod_{k=0}^{t'-1} \overleftarrow{p}(q_k)}{\prod_{k=0}^{s-1} \vec{p}(p_k) \cdot \prod_{k=0}^{t-1} \overleftarrow{p}(q_k)} \right)^2 = \sum_{t'=0}^{t-1} \left(\prod_{k=t'}^{t-1} \frac{\vec{p}(q_k)}{\overleftarrow{p}(q_k)} \right)^2 \end{aligned} \tag{C.5}$$

Both w_{s-1}^{light} and w_{t-1}^{sensor} can be iteratively evaluated. After mathematical inductions, Eq. (C.6) can be incrementally evaluated along the random walk. Then, the MIS weight (Eq. (C.2)) of any path sample is fast computed based on w_k^{light} and w_k^{sensor}.

$$\begin{aligned} w_k^{\text{light}} &= [\overleftarrow{p}(p_k)]^2 \left(\frac{1}{[\vec{p}(p_k)]^2} + \frac{w_{k-1}^{\text{light}}}{[\vec{p}(p_k)]^2} \right) \\ w_k^{\text{sensor}} &= [\vec{p}(q_k)]^2 \left(\frac{1}{[\overleftarrow{p}(q_k)]^2} + \frac{w_{k-1}^{\text{sensor}}}{[\overleftarrow{p}(q_k)]^2} \right) \end{aligned} \tag{C.6}$$

Appendix D. Upper boundary of estimate variance of $C_{\mathcal{D}_n}$

The variance of estimate of scattering order contribution $C_{\mathcal{D}_n}$ can increase if path samples $\bar{r}_{s,t}$ ($\bar{r}_{s,t}\in\mathcal{D}_n$, $s+t=n+1$) are not all independent. The MIS estimator for $C_{\mathcal{D}_n}$ and its variance are

$$F_{\mathcal{D}_n} = \sum_{s=0}^{n+1} w_{s,t}(\bar{r}_{s,t}) \cdot \frac{f^{(j)}(\bar{r}_{s,t})}{p(\bar{r}_{s,t})} = \sum_{s=0}^{n+1} F_{s,t\ (s+t=n+1)} \tag{D.1}$$

$$\mathbb{V}(F_{\mathcal{D}_n}) = \sum_{s=0}^{n+1}\sum_{s'=0}^{n+1} \mathrm{Cov}(F_{s,t}, F_{s',t'}) = \sum_{s=0}^{n+1} \mathbb{V}(F_{s,t}) + \sum_{s=0}^{n+1}\sum_{s'=0,\, s'\neq s}^{n+1} \mathrm{Cov}(F_{s,t}, F_{s',t'}) \tag{D.2}$$

With independent path samples, $\left|\mathrm{Cov}(F_{s,t}, F_{s\prime,t\prime})\right|=0 \ \ \forall s'\neq s$, then $\mathbb{V}(F_N)=\sum_{s=0}^{n+1}\mathbb{V}(F_{s,t})=\delta_{\mathcal{D}_n}^2$. When $\left|\mathrm{Cov}(F_{s,t}, F_{s\prime,t\prime})\right|>0$ the overall variance can increase. By resampling vertices on light source or sensor (*i.e.*, no re-use of already sampled vertex), the "connect to light" and "connect to sensor" methods (Figure 5) reduce path correlation. For path sample $\bar{r}_{s,t}$ of length n: $\mathrm{Cov}(\bar{r}_{0,n+1}, \bar{r}_{n+1,0}) = \mathrm{Cov}(\bar{r}_{1,n}, \bar{r}_{n,1}) = \mathrm{Cov}(\bar{r}_{0,n+1}, \bar{r}_{n,1}) = \mathrm{Cov}(\bar{r}_{1,n}, \bar{r}_{n+1,0}) = 0$ and $\mathbb{V}(F_{\mathcal{D}_1})=\delta_{\mathcal{D}_1}^2$. If $n>1$, the upper boundary of $\mathbb{V}(F_{\mathcal{D}_n})$ is computed with the Cauchy-Schwarz inequality $\mathrm{Cov}(\mathrm{X},\mathrm{Y}) \le \sqrt{\mathbb{V}(\mathrm{X})\cdot\mathbb{V}(\mathrm{Y})}$ and inequality $\sqrt{\mathbb{V}(\mathrm{X})\cdot\mathbb{V}(\mathrm{Y})} \le \frac{\mathbb{V}(\mathrm{X})+\mathbb{V}(\mathrm{Y})}{2}$.

$$\begin{aligned}\mathbb{V}(F_{\mathcal{D}_n}) &\le \sum_{s=0}^{n+1}\sum_{s'=0}^{n+1} \frac{\mathbb{V}(F_{s,t})+\mathbb{V}(F_{s',t'})}{2} - 2\left(\mathbb{V}(F_{0,n+1})+\mathbb{V}(F_{1,n})+\mathbb{V}(F_{n+1,0})+\mathbb{V}(F_{n,1})\right)\\ &= (n+2)\delta_{\mathcal{D}_n}^2 - 2\left(\mathbb{V}(F_{0,n+1})+\mathbb{V}(F_{1,n})+\mathbb{V}(F_{n+1,0})+\mathbb{V}(F_{n,1})\right)\end{aligned}$$

Hence:

$$\begin{cases}\mathbb{V}(F_{\mathcal{D}_n}) = \delta_{\mathcal{D}_n}^2, & if\ \ n=1\\ \mathbb{V}(F_{\mathcal{D}_n}) \le 2\delta_{\mathcal{D}_n}^2, & if\ \ n=2\\ \mathbb{V}(F_{\mathcal{D}_n}) \le (n+2)\delta_{\mathcal{D}_n}^2, & if\ \ n>2\end{cases} \tag{D.3}$$

Although the variance of the estimator $F_{\mathcal{D}_n}$ can increase due to correlation, it is still unbiased:

$$\begin{aligned}\mathbb{E}(F_{\mathcal{D}_n}) &= \sum_{s=0}^{n+1}\mathbb{E}(F_{s,t})_{\,(s+t=n+1)} = \sum_{s=0}^{n+1}\int_{\mathcal{D}_n} w_{s,t}(\bar{r}_n)\cdot\frac{f(\bar{r}_n)}{p(\bar{r}_n)}\cdot p(\bar{r}_n)d\mu(\bar{r}_n)_{\,(s+t=n+1)}\\ &= \int_{\mathcal{D}_n}\left(\sum_{s=0}^{n+1} w_{s,t}(\bar{r}_n)\right)\cdot f(\bar{r}_n)d\mu(\bar{r}_n)_{\,(s+t=n+1)} = \int_{\mathcal{D}_n} f(\bar{r}_n)d\mu(\bar{r}_n)\end{aligned}$$

where $p(\bar{r}_n)$ is a marginal PDF if the path samples are correlated.

Appendix E. Upper boundary of variance for radiance measurement

The methodology in appendix D can be extended to evaluate the upper boundary variance of MIS estimator for radiance measurement (Eq. (15)). Since in most optical Earth observation missions, the sensor does not see the light source (*e.g.*, sun), the contribution $C_{\mathcal{D}_1}$ is zero, and the correlation between path samples does not affect the variance of estimate for $C_{\mathcal{D}_1}$ (Eq. (D.3)). Therefore, the following discussion focuses on the impact of path sample correlation on the contributions for scattering order larger or equal to one. Then, the MIS estimator becomes:

$$F_{\mathrm{MIS}} = \sum_{n=2}^{\infty} F_{\mathcal{D}_n} \tag{E.1}$$

Eq. (E.1) is unbiased (*cf.* appendix D) even if path samples are correlated. Its variance is:

$$\mathbb{V}(F_{\mathrm{MIS}}) = \sum_{n_1=2}^{\infty} \sum_{n_2=2}^{\infty} \mathrm{Cov}\left(F_{\mathcal{D}_{n_1}}, F_{\mathcal{D}_{n_2}}\right) \tag{E.2}$$

(Kallel, 2018) shows that the contribution $C_{\mathcal{D}_n}$ decreases exponentially with the scattering order. We can suppose $C_{\mathcal{D}_{n+1}} \approx \tau \cdot C_{\mathcal{D}_n}$, τ is a constant, $0 \leq \tau \leq 1$. It is more or less true in most RT modelling for remote sensing data (Figure 17.a). It leads to: $\mathbb{V}\left(F_{\mathcal{D}_{n+1}}\right) \approx \tau^2 \cdot \mathbb{V}\left(F_{\mathcal{D}_n}\right)$.

If all the path samples are independent, the variance $\mathbb{V}(F_{\mathrm{MIS}})$ is the sum of $\delta^2_{\mathcal{D}_n}$

$$\mathbb{V}(F_{\mathrm{MIS}}) = \sum_{n=2}^{\infty} \delta^2_{\mathcal{D}_n} = \sum_{n=2}^{\infty} \tau^{2(n-2)} \cdot \delta^2_{\mathcal{D}_2} = \frac{\delta^2_{\mathcal{D}_2}}{1-\tau^2} = \delta_0^2 \tag{E.3}$$

If path samples are not all independent, the Cauchy-Schwarz inequality and Eq. (D.3) lead to:

$$\mathbb{V}(F_{\mathrm{MIS}}) = \sum_{n_1=2}^{\infty}\sum_{n_2=2}^{\infty}\mathrm{Cov}\left(F_{\mathcal{D}_{n_1}}, F_{\mathcal{D}_{n_2}}\right) \le \sum_{n_1=2}^{\infty}\sum_{n_2=2}^{\infty}\sqrt{\mathbb{V}\left(F_{\mathcal{D}_{n_1}}\right)\cdot\mathbb{V}\left(F_{\mathcal{D}_{n_2}}\right)}$$

$$= \mathbb{V}\left(F_{\mathcal{D}_2}\right) + 2\sqrt{\mathbb{V}\left(F_{\mathcal{D}_2}\right)}\sum_{n=3}^{\infty}\sqrt{\mathbb{V}\left(F_{\mathcal{D}_n}\right)} + \sum_{n_1=3}^{\infty}\sqrt{\mathbb{V}\left(F_{\mathcal{D}_{n_1}}\right)}\sum_{n_2=3}^{\infty}\sqrt{\mathbb{V}\left(F_{\mathcal{D}_{n_2}}\right)}$$

$$\le 2\delta_{\mathcal{D}_2}^2 + 2\sqrt{2}\delta_{\mathcal{D}_2}\left(\sum_{n=3}^{\infty}\sqrt{n+2}\,\delta_{\mathcal{D}_n}\right) + \sum_{n_1=3}^{\infty}\sqrt{n_1+2}\delta_{\mathcal{D}_{n_1}}\sum_{n_2=3}^{\infty}\sqrt{n_2+2}\delta_{\mathcal{D}_{n_2}}$$

$$= \delta_{\mathcal{D}_2}^2\left(2 + 2\sqrt{2}\cdot\sum_{n=3}^{\infty}\sqrt{(n+2)}\cdot\tau^{n-2} + \sum_{n_1=3}^{\infty}\sum_{n_2=3}^{\infty}\sqrt{(n_1+2)(n_2+2)}\cdot\tau^{n_1-2}\cdot\tau^{n_2-2}\right)$$

Because $\sqrt{(n_1+2)(n_2+2)} \le \frac{(n_1+2)+(n_2+2)}{2}$, $\sqrt{(n+2)\cdot 1} \le \frac{(n+2)+1}{2}$ when $n > 0$ and $\sum_{n=3}^{\infty}(n+i)\cdot\tau^{n-2} = \frac{(3+i)\tau-(2+i)\tau^2}{(1-\tau)^2}$ $(i \in \mathbb{N})$, we have:

$$\mathbb{V}(F_{\mathrm{MIS}}) \le \delta_{\mathcal{D}_2}^2\left(\frac{2+\left(6\sqrt{2}-6\right)\tau+\left(11-11\sqrt{2}\right)\tau^2+\left(5\sqrt{2}-6\right)\tau^3}{(1-\tau)^3}\right) = \left(\frac{2+\tau\left(\frac{\sqrt{2}}{2}-\tau\right)(3-\tau)}{(1-\tau)^3} + \frac{\left(\frac{9}{\sqrt{2}}-6\right)\tau+\left(14-\frac{21}{\sqrt{2}}\right)\tau^2+\left(5\sqrt{2}-7\right)\tau^3}{(1-\tau)^3}\right) \approx \delta_{\mathcal{D}_2}^2\cdot\left(\frac{2+\tau\left(\frac{\sqrt{2}}{2}-\tau\right)(3-\tau)}{(1-\tau)^3}\right) = \delta_0^{*2} \tag{E.4}$$

The term $\left(\frac{9}{\sqrt{2}}-6\right)\tau + \left(14-\frac{21}{\sqrt{2}}\right)\tau^2 + \left(5\sqrt{2}-7\right)\tau^3$ is omitted since it is less than $0.04 \ll 1$ if $\tau \in [0,1]$. Hence, the variance will increase maximally by a factor of

$$\frac{\delta_0^{*2}}{\delta_0^2} = \frac{(1+\tau)\cdot\left(2+\tau\left(\frac{\sqrt{2}}{2}-\tau\right)(3-\tau)\right)}{(1-\tau)^2} \tag{E.5}$$

In the short waves, a sensor does not usually see the light source, conversely to the long waves where the observed landscape is a light source, which implies that the contribution $C_{\mathcal{D}_1}$ to the measured radiance is usually large. Then, the same method as above shows that the variance maximally increases by the factor $\frac{\delta_0^{*2}}{\delta_0^2} = \frac{(1+\tau)\cdot\left(1+\tau^2\cdot(1-\tau^2)\cdot(2-\tau)\right)}{(1-\tau)^2}$.

751 **Reference**

752

753 Berk, A., Anderson, G.P., Acharya, P.K., Shettle, E.P., 2008. MODTRAN5. 2.0. 0 user's
754 manual. Spectr. Sci. Inc., Burlingt. MA, Air Force Res. Lab. Hanscom MA.
755 Berk, A., Bernstein, L.S., Robertson, D.C., 1987. MODTRAN: A moderate resolution model
756 for LOWTRAN. SPECTRAL SCIENCES INC BURLINGTON MA.
757 Christensen, P.H., Salesin, D.H., DeRose, T.D., Aupperle, L., 1993. A continuous adjoint
758 formulation for radiance transport, in: Proceedings of the Fourth Eurographics Workshop
759 on Rendering. Citeseer, pp. 95–104.
760 Gascon, F., Gastellu-Etchegorry, J.-P., Lefèvre, M.-J., 2001. Radiative transfer model for
761 simulating high-resolution satellite images. IEEE Trans. Geosci. Remote Sens. 39, 1922–
762 1926.
763 Gastellu-Etchegorry, J.-P., 2008. 3D modeling of satellite spectral images, radiation budget and
764 energy budget of urban landscapes. Meteorol. Atmos. Phys. 102, 187.
765 Gastellu-Etchegorry, J.-P., Demarez, V., Pinel, V., Zagolski, F., 1996. Modeling radiative
766 transfer in heterogeneous 3-D vegetation canopies. Remote Sens. Environ. 58, 131–156.
767 Gastellu-Etchegorry, J.-P., Lauret, N., Yin, T., Landier, L., Kallel, A., Malenovský, Z., Al Bitar,
768 A., Aval, J., Benhmida, S., Qi, J., 2017. DART: recent advances in remote sensing data
769 modeling with atmosphere, polarization, and chlorophyll fluorescence. IEEE J. Sel. Top.
770 Appl. Earth Obs. Remote Sens. 10, 2640–2649.
771 Gastellu-Etchegorry, J.-P., Yin, T., Lauret, N., Cajgfinger, T., Gregoire, T., Grau, E., Feret, J.-
772 B., Lopes, M., Guilleux, J., Dedieu, G., 2015. Discrete anisotropic radiative transfer
773 (DART 5) for modeling airborne and satellite spectroradiometer and LIDAR acquisitions
774 of natural and urban landscapes. Remote Sens. 7, 1667–1701.
775 Goel, N.S., 1988. Models of vegetation canopy reflectance and their use in estimation of

776 biophysical parameters from reflectance data. Remote Sens. Rev. 4, 1–212.
777 Goel, N.S., Rozehnal, I., Thompson, R.L., 1991. A computer graphics based model for
778 scattering from objects of arbitrary shapes in the optical region. Remote Sens. Environ. 36,
779 73–104.
780 Goodenough, A.A., Brown, S.D., 2017. DIRSIG5: next-generation remote sensing data and
781 image simulation framework. IEEE J. Sel. Top. Appl. Earth Obs. Remote Sens. 10, 4818–
782 4833.
783 Govaerts, Y.M., 1996. A model of light scattering in three-dimensional plant canopies: a Monte
784 Carlo ray tracing approach. Citeseer.
785 Grau, E., Gastellu-Etchegorry, J.-P., 2013. Radiative transfer modeling in the Earth–
786 Atmosphere system with DART model. Remote Sens. Environ. 139, 149–170.
787 Guillevic, P., Gastellu-Etchegorry, J.P., Demarty, J., Prévot, L., 2003. Thermal infrared
788 radiative transfer within three-dimensional vegetation covers. J. Geophys. Res. Atmos.
789 108.
790 Hosek, L., Wilkie, A., 2012. An analytic model for full spectral sky-dome radiance. ACM Trans.
791 Graph. 31, 1–9.
792 Huang, H., Qin, W., Liu, Q., 2013. RAPID: A Radiosity Applicable to Porous IndiviDual
793 Objects for directional reflectance over complex vegetated scenes. Remote Sens. Environ.
794 132, 221–237.
795 Jakob, W., 2010. Mitsuba renderer.
796 Janoutová, R., Homolová, L., Malenovský, Z., Hanuš, J., Lauret, N., Gastellu-Etchegorry, J.-
797 P., 2019. Influence of 3D spruce tree representation on accuracy of airborne and satellite
798 forest reflectance simulated in DART. Forests 10, 292.
799 Kahn, H., Marshall, A.W., 1953. Methods of reducing sample size in Monte Carlo computations.
800 J. Oper. Res. Soc. Am. 1, 263–278.

Kajiya, J.T., 1986. The rendering equation, in: Proceedings of the 13th Annual Conference on Computer Graphics and Interactive Techniques. pp. 143–150.

Kallel, A., 2018. Leaf polarized BRDF simulation based on Monte Carlo 3-D vector RT modeling. J. Quant. Spectrosc. Radiat. Transf. 221, 202–224.

Kimes, D.S., Kirchner, J.A., 1982. Radiative transfer model for heterogeneous 3-D scenes. Appl. Opt. 21, 4119–4129.

Kraska, T.A., 1996. DIRSIG: Digital Imaging and Remote Sensing Image Generation Model: Infrared Airborne Validation and Input Parameter Analysis. AIR FORCE INST OF TECH WRIGHT-PATTERSON AFB OH.

Lafortune, E.P., Willems, Y.D., 1993. Bi-directional path tracing.

Lewis, P., 1999. Three-dimensional plant modelling for remote sensing simulation studies using the Botanical Plant Modelling System. Agronomie 19, 185–210.

Myneni, R.B., Asrar, G., Gerstl, S.A.W., 1990. Radiative transfer in three dimensional leaf canopies. Transp. Theory Stat. Phys. 19, 205–250.

Myneni, R.B., Ross, J., Asrar, G., 1989. A review on the theory of photon transport in leaf canopies. Agric. For. Meteorol. 45, 1–153.

Nicodemus, F.E., 1978. Self-study manual on optical radiation measurements: Part I–Concepts, Chap. 4 and 5 p97. Nar. Bur. Stand (US). Tech. Note 910-2.

Nimier-David, M., Vicini, D., Zeltner, T., Jakob, W., 2019. Mitsuba 2: A retargetable forward and inverse renderer. ACM Trans. Graph. 38, 1–17.

North, P.R.J., 1996. Three-dimensional forest light interaction model using a Monte Carlo method. IEEE Trans. Geosci. Remote Sens. 34, 946–956.

Pharr, M., Jakob, W., Humphreys, G., 2016. Physically based rendering: From theory to implementation. Morgan Kaufmann.

Preetham, A.J., Shirley, P., Smits, B., 1999. A practical analytic model for daylight, in:

826 Proceedings of the 26th Annual Conference on Computer Graphics and Interactive
827 Techniques. pp. 91–100.
828 Qi, J., Xie, D., Yin, T., Yan, G., Gastellu-Etchegorry, J.-P., Li, L., Zhang, W., Mu, X., Norford,
829 L.K., 2019a. LESS: LargE-Scale remote sensing data and image simulation framework
830 over heterogeneous 3D scenes. Remote Sens. Environ. 221, 695–706.
831 Qi, J., Yin, T., Xie, D., Gastellu-Etchegorry, J.-P., 2019b. Hybrid Scene Structuring for
832 Accelerating 3D Radiative Transfer Simulations. Remote Sens. 11, 2637.
833 Qin, W., Gerstl, S.A.W., 2000. 3-D scene modeling of semidesert vegetation cover and its
834 radiation regime. Remote Sens. Environ. 74, 145–162.
835 Richtsmeier, S.C., Berk, A., Bernstein, L.S., Adler-Golden, S.M., 2001. A 3-Dimensional
836 radiative-transfer hyperspectral image simulator for algorithm validation, in: International
837 Symposium on Spectral Sensing Research. p. 15.
838 Sobrino, J.A., Mattar, C., Gastellu-Etchegorry, J.-P., Jiménez-Muñoz, J.C., Grau, E., 2011.
839 Evaluation of the DART 3D model in the thermal domain using satellite/airborne imagery
840 and ground-based measurements. Int. J. Remote Sens. 32, 7453–7477.
841 Thompson, R.L., Goel, N.S., 1998. Two models for rapidly calculating bidirectional reflectance
842 of complex vegetation scenes: Photon spread (PS) model and statistical photon spread
843 (SPS) model. Remote Sens. Rev. 16, 157–207.
844 Veach, E., 1997. Robust Monte Carlo methods for light transport simulation. Stanford
845 University PhD thesis.
846 Veach, E., Guibas, L., 1995a. Bidirectional estimators for light transport, in: Photorealistic
847 Rendering Techniques. Springer, pp. 145–167.
848 Veach, E., Guibas, L.J., 1995b. Optimally combining sampling techniques for Monte Carlo
849 rendering, in: Proceedings of the 22nd Annual Conference on Computer Graphics and
850 Interactive Techniques. pp. 419–428.

Wald, I., Woop, S., Benthin, C., Johnson, G.S., Ernst, M., 2014. Embree: a kernel framework for efficient CPU ray tracing. ACM Trans. Graph. 33, 1–8.

Wang, Y., Gastellu-Etchegorry, J.-P., 2021. Accurate and fast simulation of remote sensing images at top of atmosphere with DART-Lux. Remote Sens. Environ. 256, 112311.

Wang, Y., Gastellu-Etchegorry, J.-P., 2020. DART: Improvement of thermal infrared radiative transfer modelling for simulating top of atmosphere radiance. Remote Sens. Environ. 251, 112082.

Weinzierl, S., 2000. Introduction to monte carlo methods. arXiv Prepr. hep-ph/0006269.

Widlowski, J.-L., Lavergne, T., Pinty, B., Verstraete, M., Gobron, N., 2006. Rayspread: A virtual laboratory for rapid BRF simulations over 3-D plant canopies, in: Computational Methods in Transport. Springer, pp. 211–231.

Widlowski, J.-L., Mio, C., Disney, M., Adams, J., Andredakis, I., Atzberger, C., Brennan, J., Busetto, L., Chelle, M., Ceccherini, G., 2015. The fourth phase of the radiative transfer model intercomparison (RAMI) exercise: Actual canopy scenarios and conformity testing. Remote Sens. Environ. 169, 418–437.

Widlowski, J., Pinty, B., Lopatka, M., Atzberger, C., Buzica, D., Chelle, M., Disney, M., Gastellu-Etchegorry, J., Gerboles, M., Gobron, N., 2013. The fourth radiation transfer model intercomparison (RAMI-IV): Proficiency testing of canopy reflectance models with ISO-13528. J. Geophys. Res. Atmos. 118, 6869–6890.

Widlowski, J., Taberner, M., Pinty, B., Bruniquel-Pinel, V., Disney, M., Fernandes, R., Gastellu-Etchegorry, J., Gobron, N., Kuusk, A., Lavergne, T., 2007. Third Radiation Transfer Model Intercomparison (RAMI) exercise: Documenting progress in canopy reflectance models. J. Geophys. Res. Atmos. 112.

Woo, A., Pearce, A., Ouellette, M., 1996. It's really not a rendering bug, you see. IEEE Comput. Graph. Appl. 16, 21–25.

876 Woop, S., Benthin, C., Wald, I., 2013. Watertight ray/triangle intersection. J. Comput. Graph.
877 Tech. 2, 65–82.
878 Yin, T., Lauret, N., Gastellu-Etchegorry, J.-P., 2016. Simulation of satellite, airborne and
879 terrestrial LiDAR with DART (II): ALS and TLS multi-pulse acquisitions, photon
880 counting, and solar noise. Remote Sens. Environ. 184, 454–468.
881